



Microbial metallogenesis of early carboniferous manganese deposit in central Guangxi, South China

Wenchao Yu^{a,b,*}, Márta Polgári^{c,d,*}, Ildikó Gyollai^c, Krisztián Fintor^e, Heng Huang^f,
Máté Szabó^c, Yuansheng Du^{b,g}

^a State Key Laboratory of Geological Processes and Mineral Resource, School of Earth Sciences, China University of Geosciences, Wuhan 430074, China

^b Innovation Center of Ore Resources Exploration Technology in the Region of Bedrock, Ministry of Natural Resources of People's Republic of China, Guiyang 550004, China

^c Institute for Geological and Geochemical Research, Research Centre for Astronomy and Earth Sciences, ELRN, Budapest, Budaörsi str. 45, Hungary

^d Department of Natural Geography and Geoinformatics, Eszterházy Károly University, 3300 Eger, Leányka str. 6, Hungary

^e Dept. of Mineralogy, Geochemistry and Petrology, University of Szeged, 6722 Szeged, Egyetem str. 2-6, Hungary

^f Geological Team No. 4 of Guangxi Zhuang Autonomic Region, Nanning 530031, China

^g State Key Laboratory of Biogeology and Environmental Geology, School of Earth Sciences, China University of Geosciences, Wuhan 430074, China

ARTICLE INFO

Keywords:

Geomicrobiology
Baping formation
Mn-metasomatism
Rhodochrosite
Kutnohorite

ABSTRACT

Manganese deposits in the Early Carboniferous Baping Formation of central Guangxi, South China were formed in the Youjiang Basin on the southern passive margin of the South China Block. Hosted in the Second Member of the Baping Formation, the manganese ore layers were interbedded by thin-middle manganese carbonate and silicified carbonate. Previous studies provide limited information about this manganese deposit, and the sedimentary characteristics of ores and the metallogenic mechanism are not clear. In this study, integrated analyses of petrology, mineralogy, geochemistry, and carbon isotope reveal microbial metallogenesis in the Early Carboniferous manganese deposit of central Guangxi for the first time. Oncoid-bearing massive Mn carbonate and laminated Mn ore contain evidence of disseminated mineralized microbial biosignatures in millimeter scale. An *in situ* mineralogical study based on CL, FTIR, SEM-EDS and Raman spectroscopy has identified the syngenetic and diagenetic Mn and Fe systems during the formation of the manganese deposit. Both were formed by biomats and precipitated micro-laminae of microbiogenic minerals such as Mn-calcite, rhodochrosite, kutnohorite, and apatite. The metallogenic model of the manganese deposit in the Baping Formation can be divided into two main stages: (1) Sediment accumulation stage, where enzymatic Mn(II) oxidation controlled the accumulation of Mn oxides within the cyanobacterial organic and carbonate network, thus enriching the manganese; (2) Diagenetic stage, where Mn-metasomatism of microbial carbonate and the reaction between syngenetic manganese oxides and the organic matter led to the precipitation of proto-ore (Ca-rhodochrosite). A positive $\delta^{13}\text{C}$ value (+1.53‰) within the Mn carbonate sample and negative $\delta^{13}\text{C}$ values (−7.15‰ to −3.64‰) in Mn ore samples indicate the participation of organic carbon in the alkalinity source of Mn-bearing carbonates. The presence of kutnohorite and of Mn-sulfide minerals indicates a transitional zone between suboxic and anoxic conditions. Anatase represents the diagenetic mineral of Fe-biomat. After release of elements in the decomposed cells and EPS, a series of accessory minerals (feldspar, apatite, pyrite, etc.) formed.

1. Introduction

Manganese is an important element in industry and in life, and it has been considered as a good redox indicator, because manganese

enrichment is always linked with an oxic environment (Canfield et al., 2005; Roy, 2006; Maynard, 2014; Johnson et al., 2016). The first metallogenetic peak for sedimentary manganese deposits during the geological history occurred after 2.4 Ga, probably in response to the Great

* Corresponding authors at: State Key Laboratory of Geological Processes and Mineral Resource, School of Earth Sciences, China University of Geosciences, Wuhan 430074, China (W. Yu) and Institute for Geological and Geochemical Research, Research Centre for Astronomy and Earth Sciences, ELRN, Budapest, Budaörsi str. 45, Hungary (M. Polgári).

E-mail addresses: yuwenchaocug@163.com (W. Yu), rodokrozit@gmail.com (M. Polgári).

<https://doi.org/10.1016/j.oregeorev.2021.104251>

Received 3 December 2020; Received in revised form 28 April 2021; Accepted 19 May 2021

Available online 21 May 2021

0169-1368/© 2021 The Authors.

Published by Elsevier B.V. This is an open access article under the CC BY-NC-ND license

(<http://creativecommons.org/licenses/by-nc-nd/4.0/>).

Oxidation Event (Johnson et al., 2016). Previous manganese metallogenetic models provide a general framework based on the redox condition of the water mass in the basin, which controlled the formation of manganese-rich sediments (Force and Cannon, 1988; Glasby, 1988; Calvert and Pedersen, 1996; Maynard, 2003; Roy, 2006). The basic principle is that dissolved Mn^{2+} is oxidized into Mn^{4+} under oxic conditions and this precipitates as manganese (Mn^{4+}) oxides and hydroxides, completing the manganese fixation. For manganese carbonate deposits, manganese oxides and hydroxides need to be buried within the organic-rich sediments, and manganese is reduced into Mn^{2+} again during the early diagenetic stage, then combines with the CO_3^{2-} in the pore water to form manganese carbonate minerals.

Recent studies propose that the precipitation of manganese minerals usually accompanies microbial activities, including complicated biochemical and geobiological processes (Polgári et al., 2019; Gracheva et al., 2021). Manganese is an essential nutrient element for all forms of life, acting as a cofactor in various enzymes in eukaryotes, bacteria, and archaea that are important in antioxidant and metabolic functions, such as the Mn-containing superoxide dismutase, oxygenic photosynthesis, and the elimination of toxic reactive oxygen species (Ehrlich et al., 2015; Fischer et al., 2015). Some chemolithoautotrophic microorganisms, however, are able to directly obtain energy from manganese biochemical oxidation and reduction. The new discovery of manganese oxidation bacteria proves that specific microbes could oxidize coupling extracellular manganese for aerobic energy and fix autotrophic CO_2 (Yu and Leadbetter, 2020). The microbial reduction of manganese oxides has been thoroughly studied (Myers and Nealson, 1988; Lovley, 1991; Vandieken et al., 2012). Bacteria transport electrons that generated in the cytoplasm to extracellular electron acceptors via enzymatic pathways.

Previous studies mention the linkage between sedimentary manganese ore deposits and microbial activities (Ostwald, 1981; Fan et al., 1999). More detailed mineralogical and sedimentological works further reveal the significance of microbial metallogenesis in manganese deposits (Polgári et al., 2019). The Jurassic Úrkút manganese deposits in Hungary preserve abundant evidence of microbial metallogenesis, including (1) mineralized microbial fossils (Polgári et al., 2012b); (2) biogenic mineralogical variation in millimeter scale (Polgári et al., 2012a); (3) local selective enrichment of bioessential elements (Polgári et al., 2012b), and (4) low inorganic carbon isotope signatures (-5% to -10% , with the average for the Úrkút Mn deposit being -15%) which are much lighter than contemporaneous carbon isotopes recorded in seawater (Polgári et al., 2016). Besides the Úrkút manganese deposits, microbially-mediated metallogenesis has been widely reported from the manganese deposits in the Cryogenian Datangpo Formation of China (Yu et al., 2019), the Ediacaran Urucum Formation of Brazil (Biondi and Lopez, 2017; Biondi et al., 2020), and the Mesozoic Neyriz ophiolite mélange of Iran (Rajabzadeh et al., 2017).

Greater than 80% of the manganese reserves in China are hosted in sedimentary rocks, and their formation ages cover the Mesoproterozoic, Neoproterozoic, Ordovician, Devonian, Carboniferous, Permian and Triassic (Fan and Yang, 1999; Xiang et al., 2020). The Guangxi Zhuang Autonomous Region (or Guangxi for short) of South China contains $\sim 30\%$ of the manganese reserves in China. Its Devonian, Carboniferous, Permian and Triassic strata all contain manganese deposits of economic value (Xiang et al., 2020). The temporal sequence of the manganese deposits in Guangxi was the sedimentary response of the southwestern South China Block to the evolution of the Paleo-Tethys Ocean. The separation and subduction of the South China Block, North Vietnam Massif and the Indochina Block created stretched tectonic backgrounds (e.g. from the Devonian rift basin to the Triassic passive continental margin basin) which were favorable for the formation of manganese deposits (Chen et al., 2018). Previous studies on the Carboniferous manganese deposits of Guangxi have provided basic information about the tectonic background, sedimentary facies, and deposition description (Chen et al., 2018; Chen and Jiang, 2018; Huang et al., 2020). In this

study, micro-scale petrographic and mineralogical analyses and the extensive high-resolution dataset of the Carboniferous manganese deposit in the Baping Formation indicate for the first time that microbial activities played a significant role in its metallogenesis.

2. Geological setting

At least nine economically-valued Carboniferous manganese deposits have been found in the Yizhou-Liuzhou manganese metallogenetic belt (Fig. 1D); the largest one is near Xincheng County. The study section is near Limiao Village, about 20 km to the southwest of Xincheng County in central Guangxi, South China (Figs. 1 and 2). Upper Devonian to Middle Permian rocks are successively preserved in the study area, controlled by the main W-E trending anticline and a series of NW and NE trending faults (Fig. 2A). The study area was in the eastern Youjiang Basin (Fig. 1B), which went through the completed tectonic evolution (Fig. 1C). Rifting suggested to have begun in the Devonian (Huang et al., 2013). During the Carboniferous to Middle Permian, the Youjiang Basin separated the South China Block and the North Vietnam Massif. The basin represented the southwestern passive continental margin of the South China Block, continually staying in the stretched tectonic background. During the Late Permian to Early Triassic, the South China Block started to subduct beneath the North Vietnam Massif and formed the continental marginal arc on the North Vietnam Massif. After the Middle Triassic, the North Vietnam Orogenic belt formed due to the collision between the South China Block and the North Vietnam Massif, and the Youjiang Basin transited to a foreland basin. During the Carboniferous, the sedimentary feature of the Youjiang Basin showed the coexistence of shallow-water carbonate platforms and deep-water inter-platform basins (Zeng et al., 1995). Paleogeographically, Carboniferous manganese deposits were concentrated in the Yizhou rifting basin, which was the NW-trend inter-platform trough between the Northern Guangxi Platform to the north and the Central Guangxi Platform to the south (Huang et al., 2020) (Fig. 1D). Within the basin, the Carboniferous strata is composed of the Luzhai, Baping, and the lower part of the Nandan formations upwards. These are mainly siliceous rocks, black shale and carbonate rock with siliceous nodules; but in the carbonate platform area, the contemporaneous strata are the Yingtang, Huangjin, Simen, Luocheng, Dapu, Huanglong and lower part of the Maping formations from bottom to top, and they are limestone, dolostone and marlstone deposits (BGMRGZAR, 1985) (Fig. 2C). The Luzhai Formation mainly consists of thin-layer siliceous rock, mudstone, and siltstone. The Baping Formation is the manganese-bearing strata, the 1st Member is thin marlstone and interbedded siliceous rocks, the 2nd Member is the manganese-bearing part, consisting of middle-thin manganese carbonates and manganese ores, and its thickness varies from 4 m to 7 m, while the 3rd Member is middle-thick carbonate breccia. The overlying Nandan Formation is a diachronous unit, covering the interval of the late Carboniferous to early Permian; in the lower and middle parts there is middle-thin marlstone with bands and nodules of chert, and it gradually turns into dolostones in the upper part (Fig. 3).

Within the 2nd Member of the Baping Formation, four black manganese ore ($Mn > 10\%$) layers are found, which are interbedded by dark gray manganese carbonate rock ($Mn = 2\text{--}3\%$) layers. The thickness of each manganese ore layer ranges from 0.3 to 0.5 m. A previous study reported coral fossils like *Kueichouphyllum* sp., *Dibunophyllum* sp. and *Clisiophyllum* sp. in the Baping Formation, roughly constraining the deposition age to Serpukhovian-Bashkrian (Ru et al., 1992).

3. Samples

Samples were taken from the 2nd Member of Lower Carboniferous Baping Formation in the Limiao Section. The thickness of the manganese deposit is 5 m and four layers of manganese ore are preserved. Totally four typical samples were taken from the Baping Formation, including one manganese carbonate sample (MS-1) at the bottom of the

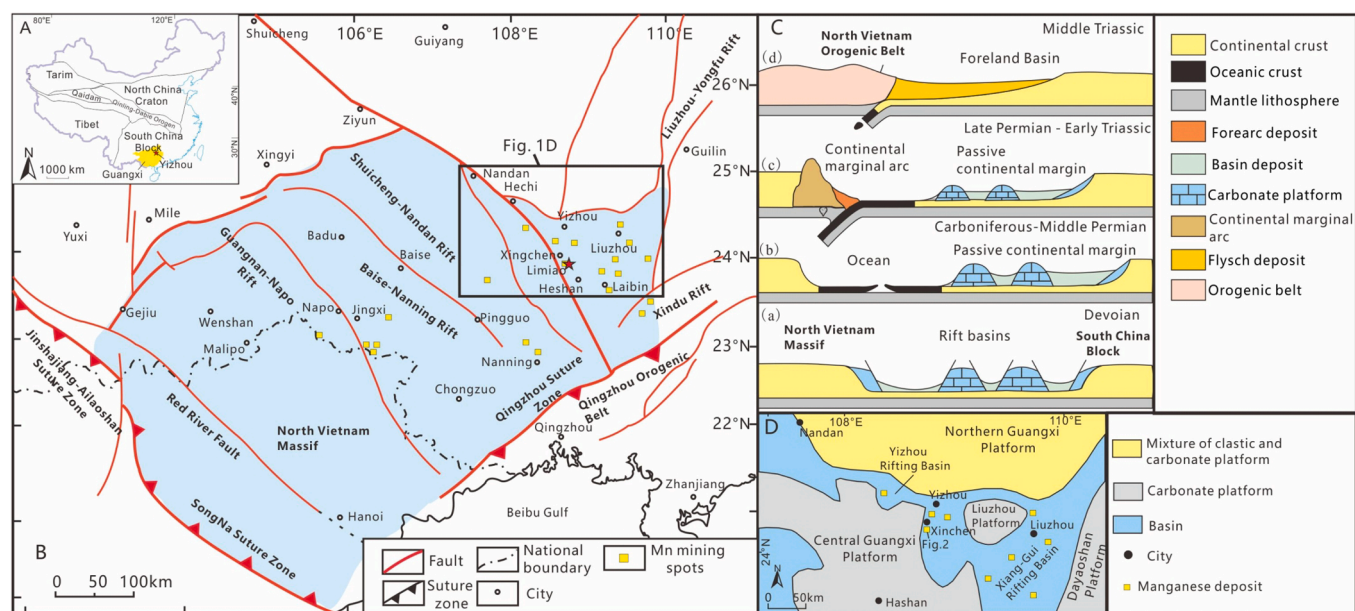


Fig. 1. A-Study area and the main mining manganese deposits in Guangxi Zhuang Autonomous Region (highlighted in yellow), South China; B-Distribution of the Youjiang Basin in South China, highlighted in light blue; C-Evolution of the Youjiang Basin from Devonian to Middle Triassic; D-Paleogeographic map of the Liuzhou-Nandan area, northern Guangxi, and Carboniferous manganese deposits in this area, modified from Huang et al. (2020).

manganese deposit and three manganese ore samples (MS-2 to MS-4) within the manganese ore layers (Fig. 3).

Sample MS-1 is a dark gray massive manganese carbonate containing concentric nodules (Fig. 4A), these nodules have irregular shapes with a diameter of 2–10 mm, and the matrix of the sample shows homogeneous texture (Fig. 4C,D). Samples MS-2 to MS-4 are finely laminated black manganese ore with pyrite lenses and laminae (Fig. 4B,E).

4. Methods

4.1. Optical rock microscopy (OM)

Petrographic studies were made on three thin sections (MS-1A, MS-1B and MS-2) in transmitted light by a NIKON SMZ800 microscope and NIKON ECLIPSE 600 rock microscope in China University of Geosciences (Wuhan) and the Institute for Geology and Geochemistry, Research Centre for Astronomy and Earth Sciences, Eötvös Loránd Research Network (IGGR RCAES, ELRN, Budapest, Hungary). In total 39 photos were taken (Table S1). The MS-1 samples do not show macroscopic lamination, which is why the thin sections were prepared on different orientations.

4.2. Cathodoluminescence (CL) observation

Cathodoluminescence (CL) petrography was carried out by a Reliotron cold cathode cathodoluminescence apparatus mounted on a BX-43 Olympus polarization microscope. Accelerating voltage was 7–7.7 keV during the analysis. Cathodoluminescence spectra were recorded using an Ocean Optics USB2000 + VIS-NIR spectrometer. Spectrometer specifications are 350–1000 nm wavelength range and 1.5 nm (FWHM) optical resolution. 48 photos were taken from three thin sections.

4.3. Electron microprobe micro-analyzer (EPMA-EDS)

Element composition and microtextural features of three thin sections were determined at 1–2 μm spatial resolution on carbon-coated sample using a JEOL Superprobe 733 electron microprobe with an INCA Energy 200 Oxford Instrument Energy Dispersive Spectrometer, run at 20 keV acceleration voltage, 6nA beam current and a count time

of 60 s for the spot measurement and 5 min for line-scan analysis. Olivine, albite, plagioclase and wollastonite standards were used; we estimated that the detection limit for the main elements was below 0.5% based on earlier measurements with various samples (IGGR RCAES, ELRN, Budapest, Hungary). 172 spectra were quarried, and 17 back-scattered electron images were made.

4.4. Fourier transform infrared spectrometer (FTIR)

Fourier transform infrared spectrometer (FTIR) was used for *in situ* micro-mineralogy and organic material identification on one thin section (105 spectra, IGGR RCAES, ELRN, Budapest, Hungary), using a Bruker FTIR VERTEX 70 equipped with a Bruker HYPERION 2000 microscope with a 20 \times ATR objective and MCT-A detector. During attenuated total reflectance Fourier transform infrared spectroscopy (ATR) analysis, the samples were contacted with a Ge crystal (0.5 μm) tip with 1 N pressure. The measurement was conducted for 32 s in the 600–4000 cm^{-1} range with 4 cm^{-1} resolution. Opus 5.5 software was used to evaluate the data and identification of minerals was based on a mineralogical database (Database of Raman – spectroscopy, X-ray diffraction, and chemistry of minerals: <http://rruff.info/>) and published references (Madejová and Komádel, 2001; Parikh and Chorover, 2006; Glotch and Rossman, 2009; Beasley et al., 2014; Müller et al., 2014). The equipment cannot be used for Mn-oxide determination because those peaks fall in the < 600 cm^{-1} range. Contamination by epoxy glue or glass was taken into consideration. 105 spectra were acquired.

4.5. Raman spectroscopy

High resolution *in situ* micro-Raman spectroscopy was used for micro-mineralogy and organic matter identification on 3 thin sections and 5 profiles (profile L1-L1' in MS-1A, profiles L2-L2' and L3-L3' in MS-1B, profile L4-L4' and L5-L5' in MS-2, Fig. 4), resulting in a total of 7677 spectra. A Thermo Scientific DXR Raman Microscope was used, with a 532 nm (green) diode pumped solid-state (DPSS) Nd-YAG laser using 1.5 mW laser power, 50 \times objective lens in confocal mode (confocal aperture 25 μm slit). Acquisition time was 1 min and spectral resolution was $\sim 2 \text{ cm}^{-1}$ at each measurement (University of Szeged, Hungary); the distance between each point was 10 μm and the measurement time was

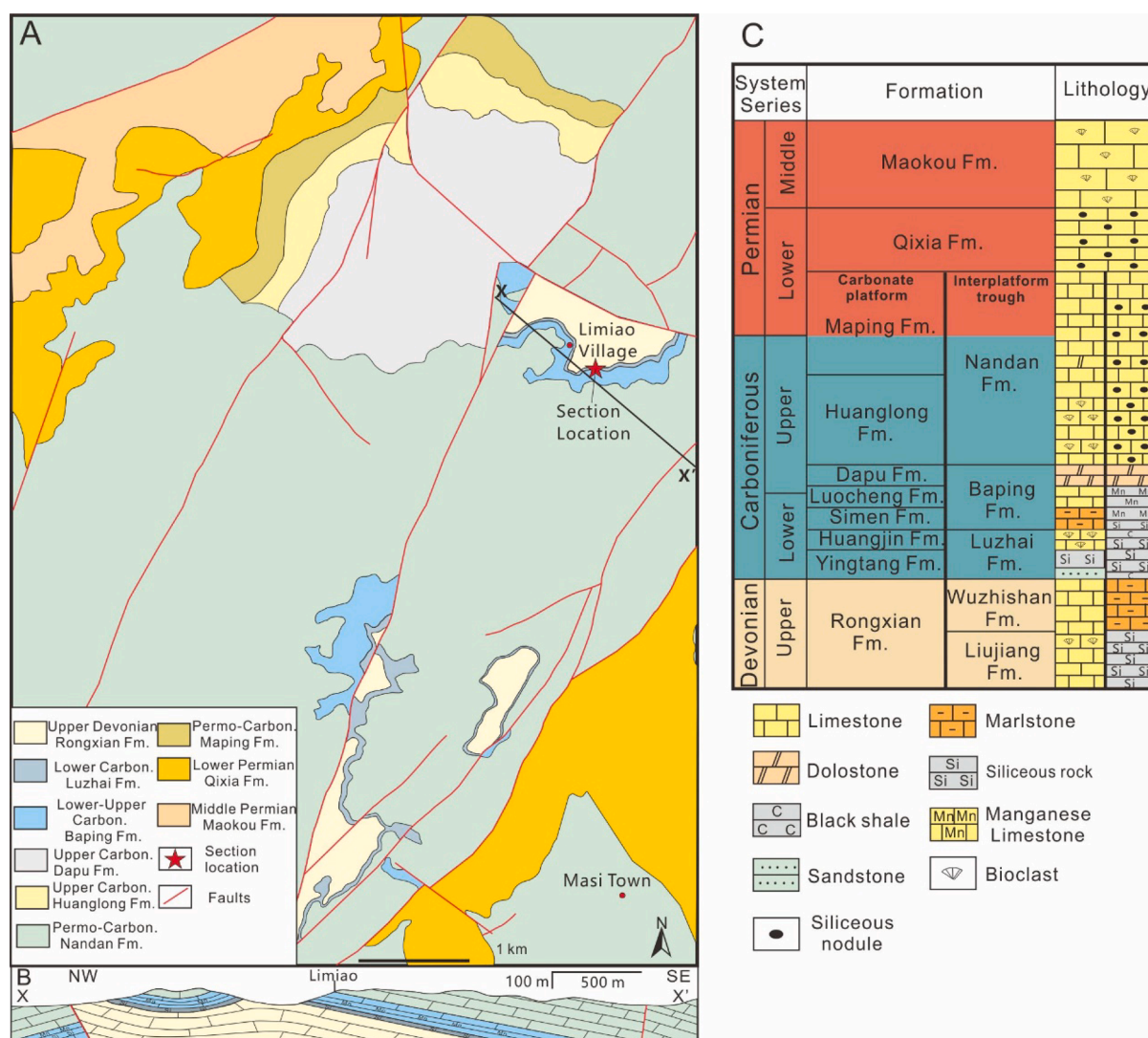


Fig. 2. A- Geological map of the study area (Masi-Limiao area) in central Guangxi Zhuang Autonomous Region; B-cross section of the x-x' line in Fig. 2A; Fig. 2C- Lithological column showing the sedimentary differentiation in the Youjiang Basin during the Late Devonian to Middle Permian.

10 min. A composite image of thin sections of Raman microscopy measurements and series of Raman spectra acquired along the vertical sections is indicated in thin section photos on Fig. 4 (arrow points to measurement direction). Diagrams were organized by peak height versus analytical spot number of each of the phases along the Raman scanned section. Intensities were normalized to the highest peak for each spectra.

The spectra were elaborated in two ways:

(1) Diagrams were organized in terms of peak height versus analytical spot number of each of the phases along the Raman scanned section (main minerals and organic matter in general). (2) A detailed determination of all spectra was also made. These results are summarized in Table S2.

Aside from the profile analyses, descriptions of the mineral phase transitions were also constructed for clarification of rhodochrosite (Mn-bearing calcite)/kutnohorite (one photo, one profile). The following Raman bands were used for normalization: rhodochrosite: $\sim 1086 \text{ cm}^{-1}$, kutnohorite: $\sim 1083 \text{ cm}^{-1}$, ankerite/dolomite: $\sim 1093\text{--}96 \text{ cm}^{-1}$, apatite: $\sim 965 \text{ cm}^{-1}$, quartz: $\sim 463 \text{ cm}^{-1}$; carbonaceous matter: $\sim 1605 \text{ cm}^{-1}$. Identification of minerals was based on the RRUFF Database and the following references (Orange et al., 1996; Julien et al., 2004; Frost et al., 2005; Chen et al., 2007; Jehlička et al., 2009; Das and Hendry, 2011; Baoumy et al., 2013; Jones et al., 2013; Fernandez et al., 2015; Okolo

et al., 2015; Sepúlveda et al., 2015; Lafuente et al., 2016), please see Table S2 for details. Contamination by epoxy glue was taken into consideration. The sensitivity of FTIR is better than that of Raman spectroscopy for organic matter.

4.6. Whole rock geochemistry and microanalysis (XRF)

Whole rock elements analyses were carried out by the ALS Chemex Laboratory (Guangzhou, China) on four samples from the Limiao Section. Each whole-rock sample was crushed in a corundum jaw crusher (to 60 mesh) and then powdered in a tungsten carbide ring mill to finer than 200 mesh. Major-element measurements were made using a Shimadzu 1800X X-Ray fluorescence (XRF) unit with a detection limit of 0.1–1 ppm and an analytical precision better than $\pm 3\%$ of reported values. Loss-on-ignition (LOI) was used to determine total volatile content. Trace element and rare earth element (REE) content was analyzed using an inductively coupled plasma-mass spectrometer (ICP-MS). Powdered samples were placed in Teflon bombs and moistened with a few drops of ultrapure water. Then, 1.5 ml HNO_3 and 1.5 ml HF were added to the sample powder. The sealed Teflon bombs were heated at 190°C in an oven for 48 h. Then sample solutions were evaporated on a hot plate at $\sim 115^\circ \text{C}$ to dryness. This was followed by adding 1 ml HNO_3 and evaporating to dryness a second time. The resultant salt was

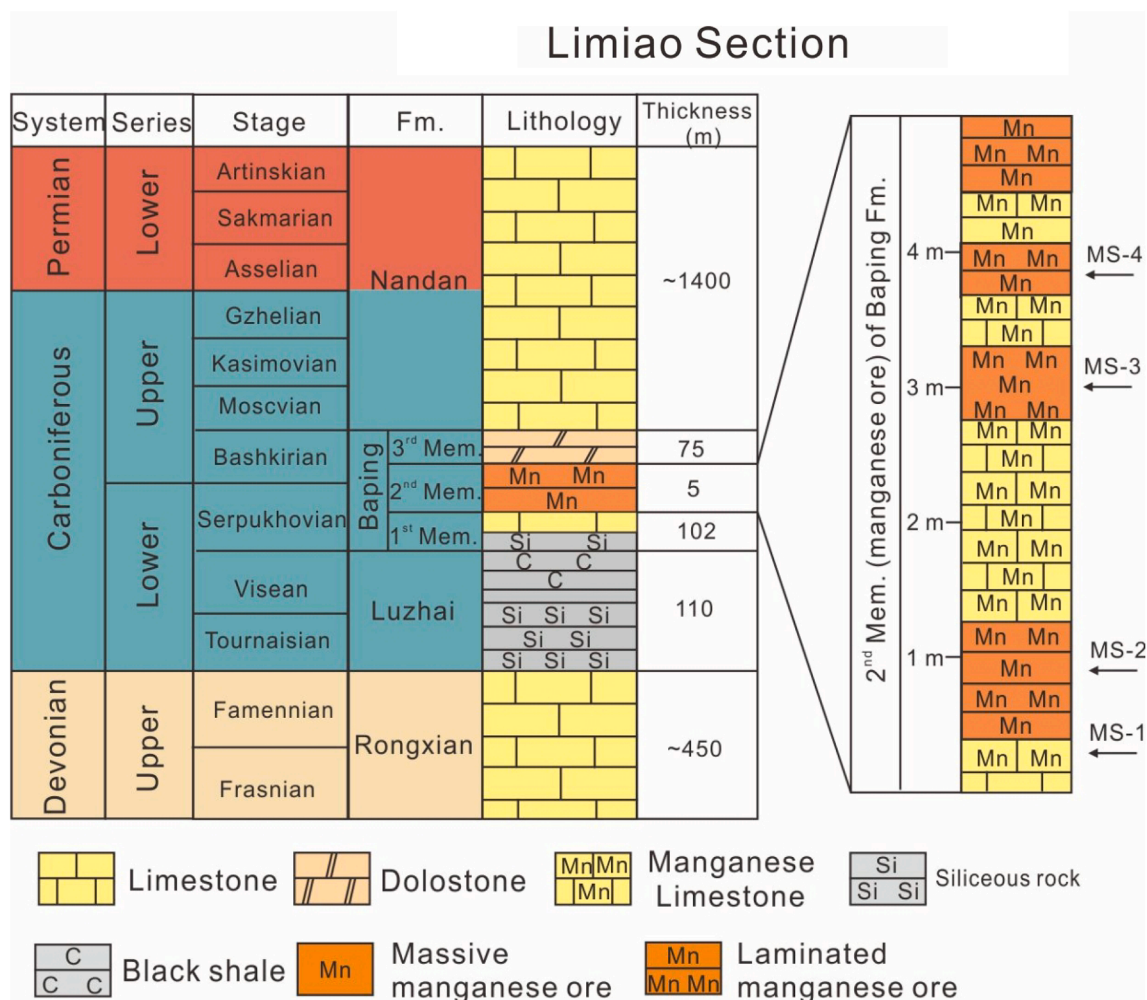


Fig. 3. Carboniferous stratigraphic frame in the study area and the structure of the manganese deposit in the 2nd Member of the Baping Formation.

re-dissolved by adding ~3 ml of 30% HNO₃ and resealed and heated in the bomb at 190 °C for 24 h. The final solution was diluted with distilled water to ~100 mg prior to analysis. The detection limit for individual trace elements and REEs ranged from 2 to 8 ppm. All concentrations are given as weight percent (wt. %). Data are summarized in Table S3.

Energy dispersive (EDS) X-ray fluorescence analysis was carried out on thin sections using a Horiba Jobin Yvon XGT 5000 X-ray fluorescence microscope (University of Szeged, Hungary). Measurement conditions were 50 kV beam voltage, 0.1 mA beam current, and 10 μm beam spot diameter. Every single analyzed area was 1 mm × 5.124 mm along a line (the longer side of the analyzed area was parallel with the line in each case) perpendicular to the lamination of the sample. Analyzed areas were divided into 512 × 100 pixels with a pixel size of 0.01 mm². The intensity of each element was measured in count per seconds (cps). The method was used for clarification of carbonate types.

4.7. Stable C and o isotope study

The isotopic composition of δ¹³C and δ¹⁸O was measured on carbonates (rhodochrosite, kutnohorite, calcite, n = 4) and organic matter (n = 4) using a Finnigan Delta V continuous-flow mass spectrometer equipped with a Thermo Flash element analyzer (IGGR RCAES, ELRN, Budapest, Hungary). Three sets of samples were measured for comparison. Results are given in per mil (‰) versus V-PDB (δ¹³C) and SMOW (δ¹⁸O) standards (Table S3). Standard deviation of the data is below 0.1‰ based on the reproducibility of sample triplets and laboratory standard data. Measurements in the case of carbonate were organic matter free

and in the case of organic matter they were carbonate free.

5. Results

The results of the investigation into sections are presented based on the methods used.

5.1. Optical microscopy (OM) results

Sample MS-1 and the thin sections made from this sample (MS-1A, MS-1B) do not show either macroscopic or microscopic lamination (Figs. 4 and 5). Detritus material is not found. Diagenetic sedimentary features are common in the form of oncoides, nodules with brownish encrustation. Coarse calcite precipitation was detected. Randomly disseminated mineralized microbial biosignatures are common (Fig. 5A–D). The matrix is very fine-grained obscure (Fig. 5B). Rarely a weak brownish biomat structure occurred (Fig. 5C,D).

Sample MS-2 is finely laminated, containing pyrite laminae and nodules, nodules were compressed to oval shape (Fig. 5G). The pyrite grains are angular (rhombohedral) and their surface is inhomogeneous. The size of the angular pyrite grains is around 10–20 μm (Fig. 5H). The grains form larger clusters of some hundreds of μm. The matrix is very fine grained, obscure, and detritus material is not visible.

5.2. Cathodoluminescence (CL) observations

In sample MS-1, Mn-bearing calcite and kutnohorite (mixed

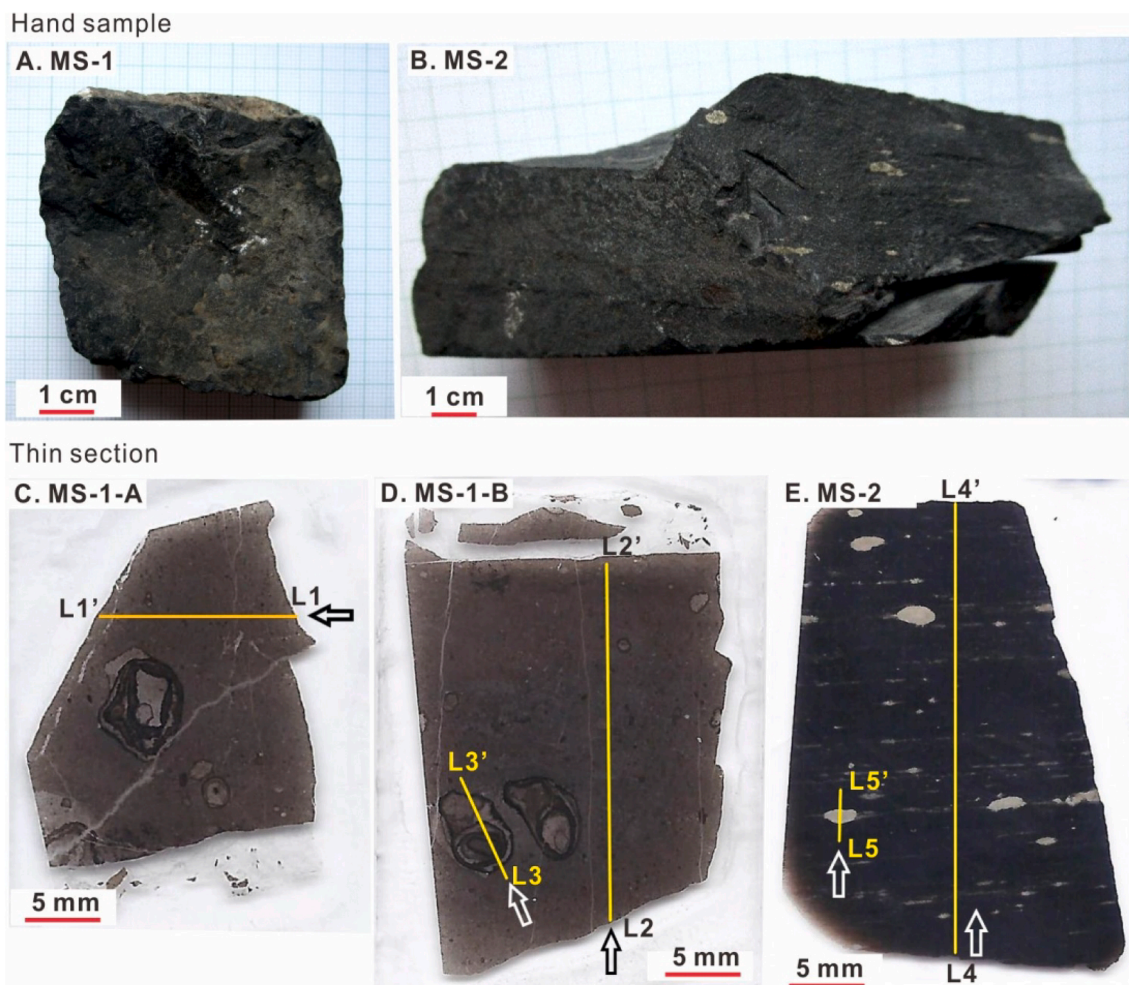


Fig. 4. A and B-hand samples of sample MS-1 and MS-2; C, D and E are thin sections of analyzed samples, yellow lines of L1-L1' to L5-L5' indicate the scan paths of Raman spectra measurement. Notice the massive structure and nodules in the MS-1 samples and laminated structure in MS-2 sample.

carbonate) show bright orange luminescence (Fig. 6A–D). The crusted oncooids contain an inhomogeneous inner structure with one encrustation or complex encrustation (Fig. 6A,C), but they show similar homogenous bright orange luminescence, indicating minerals of oncooids are compact carbonates (Fig. 6B,D). The small differences in CL may reflect the transitional mineral phase of mixed carbonates. Late diagenetic or younger vein fillings are clearly visible in this sample (Fig. 6C, D). The orange veins and the other luminescent phases are most probably diagenetic Mn-bearing calcite and kutnohorite (Polgári et al., 2007). The matrix is obscure by rock microscopy and includes small spherical or oval forms, which often have a concentric inner structure (Fig. 6A). The matrix material is fluffy, resembling mineralized microbial biosignatures. The CL is bright orange as in the case of oncooids, and the marginal part of the spherical forms is often covered by wolf-tooth diagenetic carbonate overgrowth. These spherical forms occur in very fine-grained material, which has dim orange luminescence. Bright orange luminescence is common in case of low Fe-bearing carbonates caused by Mn^{2+} as activator elements (Polgári et al., 2007). CL images show detritus was not the dominant phase in this sample.

Sample MS-2 shows that microbialite networks include small mineral grains, which show bright orange, reddish luminescence (Fig. 6E,F). The matrix of sample MS-2 may be non-luminescent rhodochrosite. Rarely grains with greenish-yellow luminescence can be observed (probably apatite). Bluish segregated quartz rarely occurs. Detritus was not detected by CL as a dominant phase.

5.3. Electron probe micro-analyzer (EPMA–EDS) results

Manganese carbonate sample (MS-1) analyses show mixed carbonate phase, with Ca, Mn, Mg and in some cases Fe occurring (Fig. 7A), and moderate Mn content present in grains and matrix. Microbial carbonate biosignatures are also present in the microcrystalline carbonate matrix. The Mn infiltration (metasomatic process) is oriented from the matrix toward the biosignatures. Some marginal parts are enriched in Mn, which supports metasomatism origin. Early diagenetic rhombohedral carbonate minerals (dolomite-like) occur. Concerning the heterogeneous carbonate composition, a CaO–MnO–MgO triangle diagram was produced based on the EDS data (Fig. 8). Mn- and Mg-bearing calcite occurs with randomly variable contents, while rhodochrosite was rare (only one data point in MS-1). Some double-mixed carbonates probably occur. Silica content is low or absent, and pyrite is rare (with As, Co, Ni, Zn, Cu-traces). Apatite, feldspar and barite are also observed.

Sample MS-2 contains more Mn-rich minerals than Sample MS-1, and Ca-bearing rhodochrosite, kutnohorite can be identified in the EDS scanning images (Fig. 7B). Mg content is also higher and randomly variable. Silica is segregated based on micro-textural features, and its content is considerable. Apatite is moderate. The sample is pyrite-rich (laminae), and in some cases pyrite contains As, and trace Co, Ni, Zn, Cu.

5.4. Fourier transform infrared spectroscopy (FTIR) results

A total of 105 FTIR spectra were taken at 14 parts of thin sections (Fig. 9). The photos at all measuring parts show the points where spectra

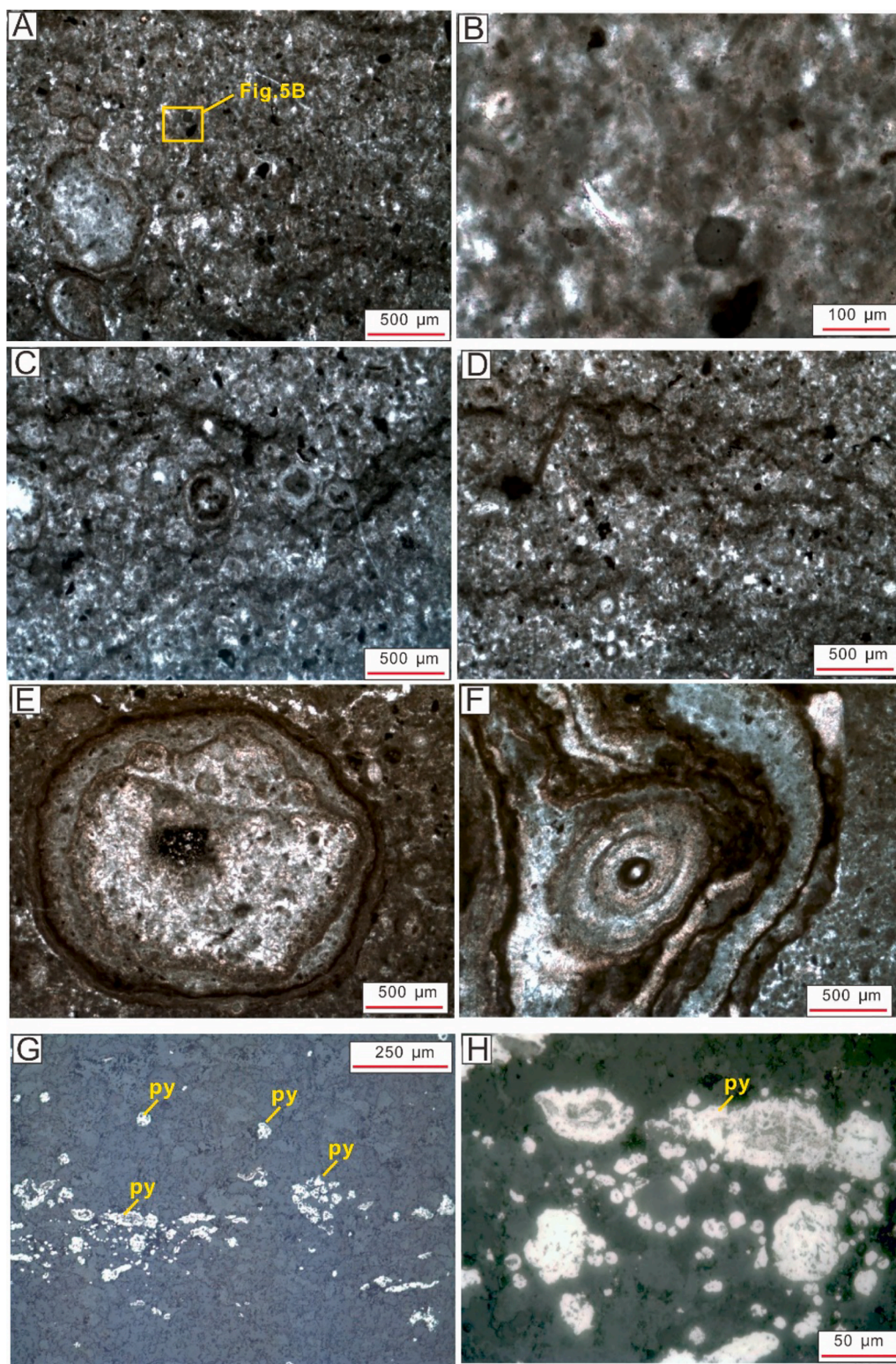


Fig. 5. Optical microscope photos (A-F transmitted light, 1 N, G-H reflected light, 1 N) of Mn-bearing carbonate (MS-1) and Mn ore (MS-2) samples. A- micrometer-scale nodules and microlithic matrix in MS-1 sample; B- enlargement of marked area in Fig. 5A, showing microlithic matrix and amorphous organic materials; C and D- micrometer-scale nodules and biomat-like weak laminated texture in MS-1 sample; E- inner structure of the millimeter-scale oval nodule in MS-1 sample, showing the stratified structure with black core, white mantle, and black crust; F- concentric texture within the nodule of MS-1 sample; G and H- weak laminated structure in MS-2, massive and framboidal pyrites (py) can be observed.

were taken, and mineral phases in samples are listed in Table S4. According to the FTIR analyses, the samples are very fine grained, fluffy, and detritus minerals were rarely detected. The main Mn mineral is rhodochrosite, although other carbonate minerals such as siderite and dolomite also occurred. Fe oxide-hydroxide as ferrihydrite and hematite and locally pyrite was determined, with ferrihydrite occurring in the vicinity of pyrite. In sample MS-2 the organic matter is frequent. Associated minerals apatite, feldspar (albite), and quartz were detected. It

seems that feldspar also occurs as a very fine grained component, similarly to other mineral phases.

5.5. Raman spectroscopy results

A total of 7677 spectra were determined for micro-mineralogical and organic matter composition and also for the distribution of minerals and organic matter according to the five profiles of three thin sections (MS-

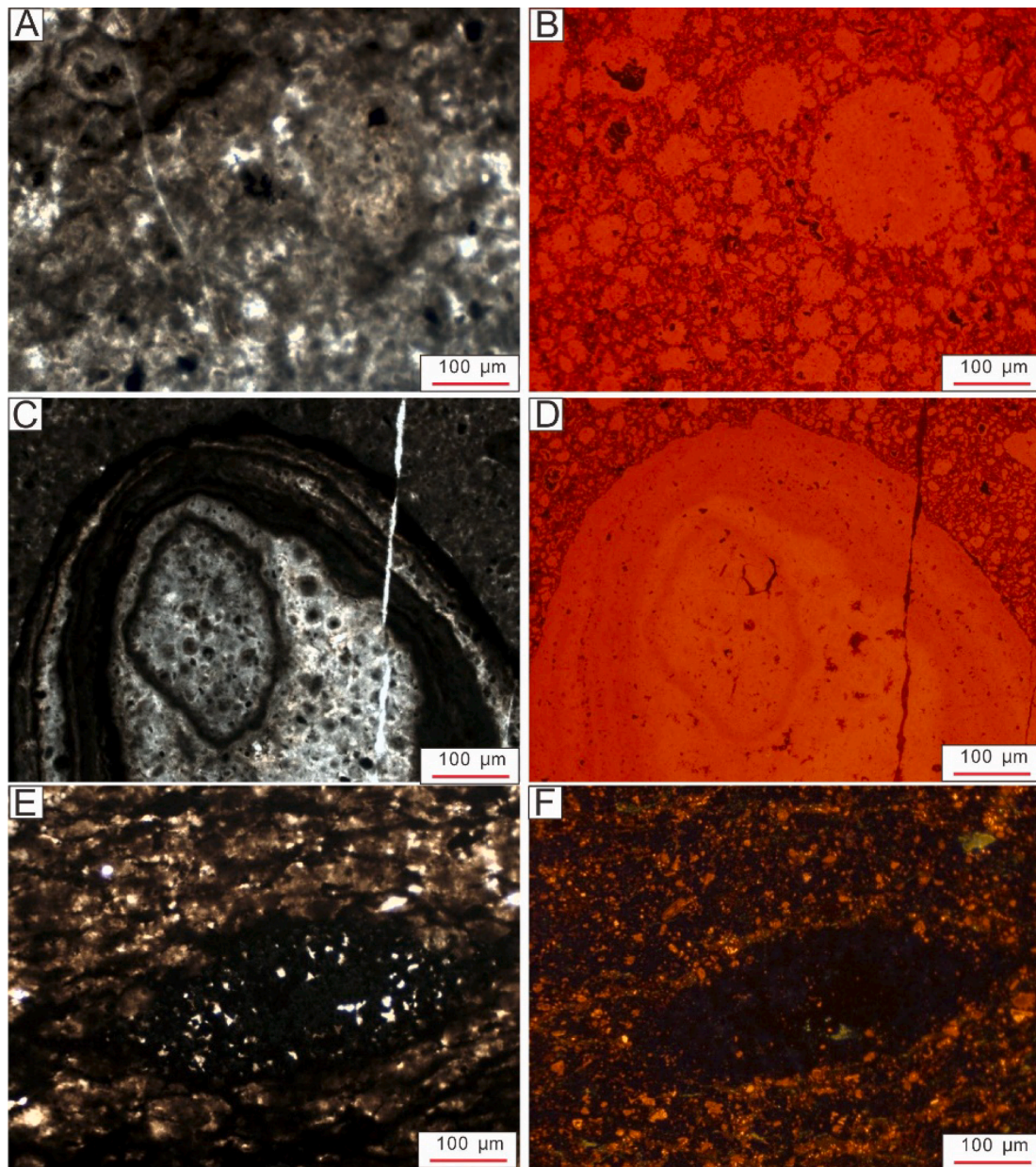


Fig. 6. Optical microscope and cathodoluminescence (CL) photos of sample MS-1 (A, B, C and D) and MS-2 (E, F). Transmitted light (1 N) photos (A, C, E) and CL photos (B, D, F).

1A, MS-1B and MS-2, Fig. 4C–E). The analyzed profiles are shown in Fig. 4. The main mineral distribution was evaluated visually based on series of Raman profiles using 10 μm scale (Figs. 10–13). Rhodochrosite/calcite (calcite structure), kutnohorite (double carbonate structure), quartz, pyrite, apatite, feldspar, anatase, and carbonaceous material were detected.

In sample MS-1A (Fig. 10) and MS-1B (Fig. S1 and S2) carbonate minerals and carbonaceous matter are the two main components. Calcite/rhodochrosite and kutnohorite are identified as the dominating carbonate minerals. Based on the result of the EPMA-EDS results, rhodochrosite is rare in this sample, but Mn-bearing calcite and calcite are widespread. A negative correlation of the contents of calcite/rhodochrosite and kutnohorite can be observed from micron-scale cyclic variations of the curves (Fig. 10). The carbonaceous matter is high in the sample, a positive correlation can be observed between the carbonaceous matter and calcite/rhodochrosite, whereas a negative correlation is presented between the carbonaceous matter and kutnohorite.

The oncoide in sample MS-1 is analyzed by the profile L3-L3' with length of 8.45 mm (Fig. 4D), and results show that oncoides were affected by stronger diagenesis than matrix. Rhodochrosite is the dominant mineral, kutnohorite is less than in the matrix, and the alternating cycles of rhodochrosite and kutnohorite still remain. Particularly, 31 quartz cycles join the system, including four large peaks and 27 small peaks, with quartz peaks frequently coinciding with kutnohorite peaks. Content of carbonaceous matter in the oncoide shows more complex variations than in the matrix. Based on the mineralogical variation, the profile L3-L3' can be divided into three parts (Fig. S2): (1) the rim of oncoide (0–800 μm), rhodochrosite and kutnohorite show variations in content, carbonaceous matter maintains relatively low content; (2) the core of oncoide (800–6800 μm), rhodochrosite is the dominant mineral with decreasing kutnohorite, and cycles of rhodochrosite and kutnohorite still remain. The negative correlation between carbonaceous matter and rhodochrosite is obvious; (3) the rim of oncoide (6800 μm to end), this part shows the same features as Part 1.

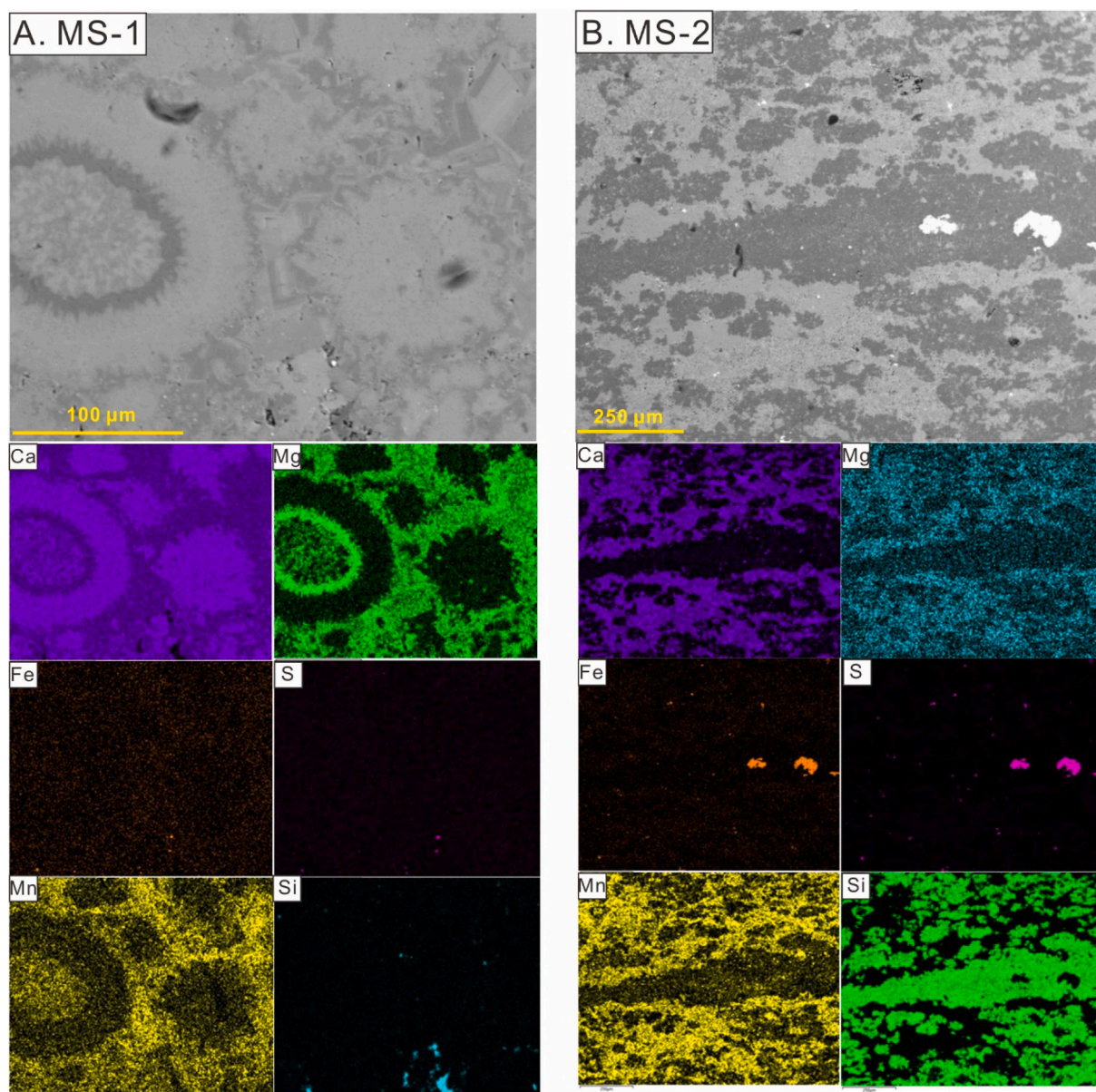


Fig. 7. SEM-EDS back-scattered images and EDS elements scanning images of A-MS-1 sample and B-MS-2 sample. Analyzed elements included Ca, Mg, Fe, S, Mn and Si. More results please see [Supplementary materials](#).

Sample MS-2 is macroscopically laminated, and results of Raman spectroscopy (profile L4-L4' in [Fig. 4E](#)) reveal that these laminae are micron-scale cycles of carbonates and quartz ([Fig. 11](#)). The content of carbonaceous matter is high, pyrite and anatase also show several independent peaks. In the profile L5-L5' of the mineralogical section for the pyrite nodule ([Fig. 12](#)), pyrite is the dominant mineral, while carbonaceous matter shows a negative correlation with the pyrite. Carbonates show some peaks within the pyrite nodule, and anatase and quartz are represented by cycles of small intensities in the whole profile with some elevated peaks ([Fig. S3](#)).

5.6. Whole rock geochemistry and C-O isotopes

The Mn carbonate sample (MS-1) and the Mn ore samples (MS-2, MS-3, and MS-4) from the Limiao section exhibit distinctive geochemical and isotopic characteristics ([Table S3](#)). The Mn carbonate sample contains high CaO (43.70%) and MgO (6.35%), moderate MnO (5.00%) and low Al₂O₃ (0.11%), SiO₂ (0.82%), and TFe₂O₃ (0.06%). The Mn ore

samples contain high MnO (14.65–32.0% with a mean of 24.22%), moderate CaO (14.00–19.25% with a mean of 17.48%), MgO (2.04–5.43% with a mean of 3.89%) and TFe₂O₃ (0.68–3.46% with a mean of 1.76%), variable SiO₂ (1.93–40.83%), and low Al₂O₃ (0.16–0.42% with a mean of 0.30%). As to trace elements, the Mn carbonate sample contains relatively low content of some trace elements (e. g., Cr, Ni, Mo, U, V, Zn and Zr) and low content of ΣREE + Y compared to Mn ore samples ([Table S3](#)).

Total organic carbon (TOC) and the carbon and oxygen isotope data for the present study section are given in [Table S3](#). TOC in the Mn ore samples is 0.49–1.17% with a mean of 0.79%, the Mn carbonate sample contains TOC of 0.07%. Inorganic carbon isotope ($\delta^{13}\text{C}_{\text{carb}}$) values of the Mn ore samples range from -7.15‰ to -3.64‰ , while $\delta^{13}\text{C}_{\text{carb}}$ values of the Mn carbonate sample is high ($+1.53\text{‰}$). Organic carbon isotope ($\delta^{13}\text{C}_{\text{org}}$) and oxygen isotope ($\delta^{18}\text{O}_{\text{SMOW}}$) values of the Mn ore samples (-21.05‰ to -20.23‰ for $\delta^{13}\text{C}_{\text{org}}$, $+30.2\text{‰}$ to $+31.5\text{‰}$ for $\delta^{18}\text{O}_{\text{SMOW}}$) are heavier than those of the Mn carbonate sample (-21.55‰ for $\delta^{13}\text{C}_{\text{org}}$, $+28.00\text{‰}$ for $\delta^{18}\text{O}_{\text{SMOW}}$).

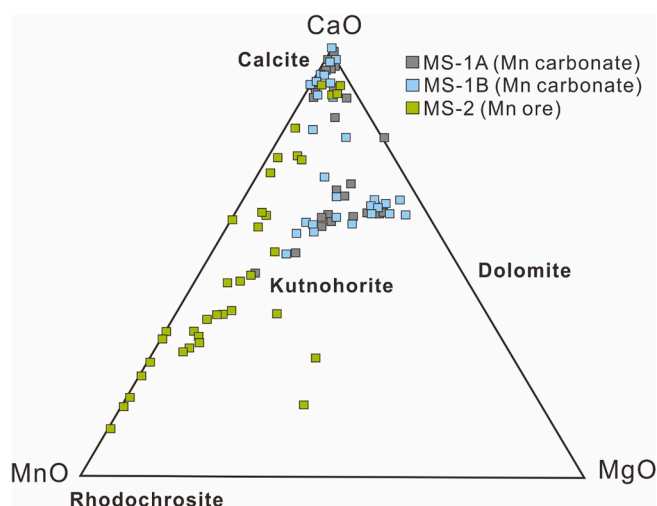


Fig. 8. CaO-MnO-MgO triangle diagram for the SEM-EDS analyses of samples MS-1A, MS-1B and MS-2.

6. Discussion

6.1. Microbial systems and formation stages in manganese ore deposits

6.1.1. Overview of the two-step microbial ore formation mechanism

Microbially-mediated manganese ore-forming systems have been widely reported in the global manganese deposits. Based on case studies, a two-step microbial manganese ore formation mechanism has been proposed (Polgári et al., 2012b). This two-step microbial ore formation mechanism can be divided into two stages: (1) Oxidization stage: a chemolithoautotrophic stage under oxic-suboxic conditions, which in the case of manganese precipitates metal ions from the aquatic system to solid oxide/hydroxide form; (2) Reduction stage: a heterotrophic stage under anoxic-suboxic conditions forming Mn-bearing and/or Fe-bearing carbonates (e.g., Mn-calcite, rhodochrosite, ankerite and siderite).

The existence of a two-step microbial manganese ore formation process is supported by recent geobiologic manganese cycle research. Although the pathway of microbial Mn(II) oxidation has long been discovered (Mandernack et al., 1995; Bargar et al., 2005; Canfield et al., 2005; Tebo et al., 2005; Ehrlich et al., 2015), only recently did researchers find that the existence of chemolithoautotrophic microorganisms depends on coupling extracellular Mn(II) oxidation to aerobic energy conservation and autotrophic carbon fixation (Yu and Leadbetter, 2020). This discovery reverses the previous belief that manganese oxidizers are all organoheterotrophs, gaining no energy from manganese oxidation (Canfield et al., 2005). For microbial manganese reduction, microorganisms that are strict or facultative anaerobes are able to reduce Mn (III, IV) oxides in an anaerobic respiratory process (Nealson and Saffarini, 1994; Ehrlich et al., 2015). So far, two different general strategies have been identified for microbial Mn reduction: (1) Direct (enzymatic) reduction via cytochromes. At least two enzymatic pathways are found in bacteria, both of which are able to transport electrons generated in the cytoplasm to extracellular electron acceptors via multiple c-type cytochromes (Lovley, 1991; Lin et al., 2012); (2) Indirect (nonenzymatic) reduction. Some bacteria and most fungi likely could excrete metabolic products that are strong enough reductants for Mn (VI) oxides.

6.1.2. Syngenetic and diagenetic Mn and Fe systems in the Carboniferous manganese deposit of central Guangxi

New evidence acquired from the Early Carboniferous manganese deposits in central Guangxi, South China indicate that microbial activities played an important role during the formation of the manganese carbonates and ores. Microtextural evidence in all of the studied samples

appears as dense features, and the mineral types and embedded variable organic matter raise the possibility of the microbially-mediated formation of the ore beds, which we argue occur as microbialites. Two microbial ore forming systems are proposed as dual systems, characterized by Fe- and Mn-oxidizing metabolic processes, probably linked to Fe- and Mn-oxidizing bacteria, respectively. Besides these, strong cyanobacterial activities may accompany the manganese ore-forming processes, which led to the precipitation of carbonate (Mn-calcite and calcite) minerals.

Syngenetic as well as diagenetic minerals were preserved, as identified by the Raman and FTIR analyses. Along with hydrocarbons, these analyses identified minerals such as todorokite, manganite and ferrihydrite, and lepidocrocite, which we consider remnants of the original sedimentation. Remnants of syngenetic and diagenetic minerals as complex systems give a reasonable series of processes and environmental formation conditions during sedimentation and diagenesis. The paleoenvironmental outlook is based on mineral assemblage and summarized in Table S5. Main minerals form the ore beds, but the moderate and minor minerals also have genetic importance. The Mn layers are the result of complex diagenetic processes and the formation of diagenetic minerals, which include the components of the decomposition of cells and extracellular polymeric substance material (Fe and Mn bacteria, cyanobacteria, and other types; see Ewers, 1983; Konhauser, 1998; Wignall and Newton, 1998; Dupraz and Visscher, 2005; Dupraz et al., 2009; Chan et al., 2011; Gyollai et al., 2017; Polgári et al., 2019; and Biondi et al., 2020).

6.1.2.1. Remnants of syngenetic minerals. Some syngenetic poorly crystallized minerals were preserved in the samples; they are microbially-mediated minerals forming under obligatory oxic (Mn) and suboxic (Fe) conditions, with neutral and semi-neutral pH. Cyanobacterial carbonate formation occurs in photic zone under suboxic, semi-neutral pH. The microbially-mediated Mn and Fe oxidation have different oxygen demand, and the diagenetic zones represent different oxygen conditions. For more details see Biondi et al. (2020).

6.1.2.2. Syngenetic Mn system. Manganese carbonate and manganese ore samples in the Early Carboniferous Baping Formation of central Guangxi, South China provide an opportunity to reconstruct the transition from the low-Mn carbonate to the high-Mn ore during the metallogenesis. Regular enzymatic Mn^{2+} oxidation is considered to be the most important mechanism for the precipitation of Mn-bearing minerals. Mn-oxide formation during the development of the Mn-oxide proto-ore, the first product of microbial enzymatic Mn(II) oxidation, probably was a bio-oxide (e.g., todorokite, manganite), similar to the experimental studies of Villalobos et al. (2003), Bargar et al. (2005) and Bodei et al., 2007. This enzymatic Mn oxidation can be referred to as the first stage of the two-step microbial ore formation mechanism. The demand of microbial (enzymatic) Mn(II) oxidation is obligatory oxic conditions (>2 ml/L dissolved oxygen) (Villalobos et al. 2003). This bio-oxide is an X-ray amorphous oxide similar to δ - MnO_2 (todorokite, manganite; both detected by Raman in the current study). A decrease in the dissolved Mn(II) appears to act as a reductant for the biogenic oxide and to control the stability of secondary abiotic reaction products (Mn^{2+} components in minerals of MS-1A support this process). Cation binding, like Mg, supports phyllosilicate transformation to stable tecto-manganate (Bodei et al. 2007). Experimental studies showed that extracellular polymers from bacteria catalyze the adsorption of Mg on the surface of the cells (Mandernack et al. 1995). Thus, the bacterial cells not only directly oxidize Mn(II) to Mn(IV), but also, in the early stages of oxidation, influence the cation composition of the Mn-oxide mineral being produced.

Based on this study, alternative pathways of Mn-bearing carbonate precipitation including the Mn-metasomatism of calcite and the primary rhodochrosite formation can be proposed. Jurassic Mn-carbonate ore

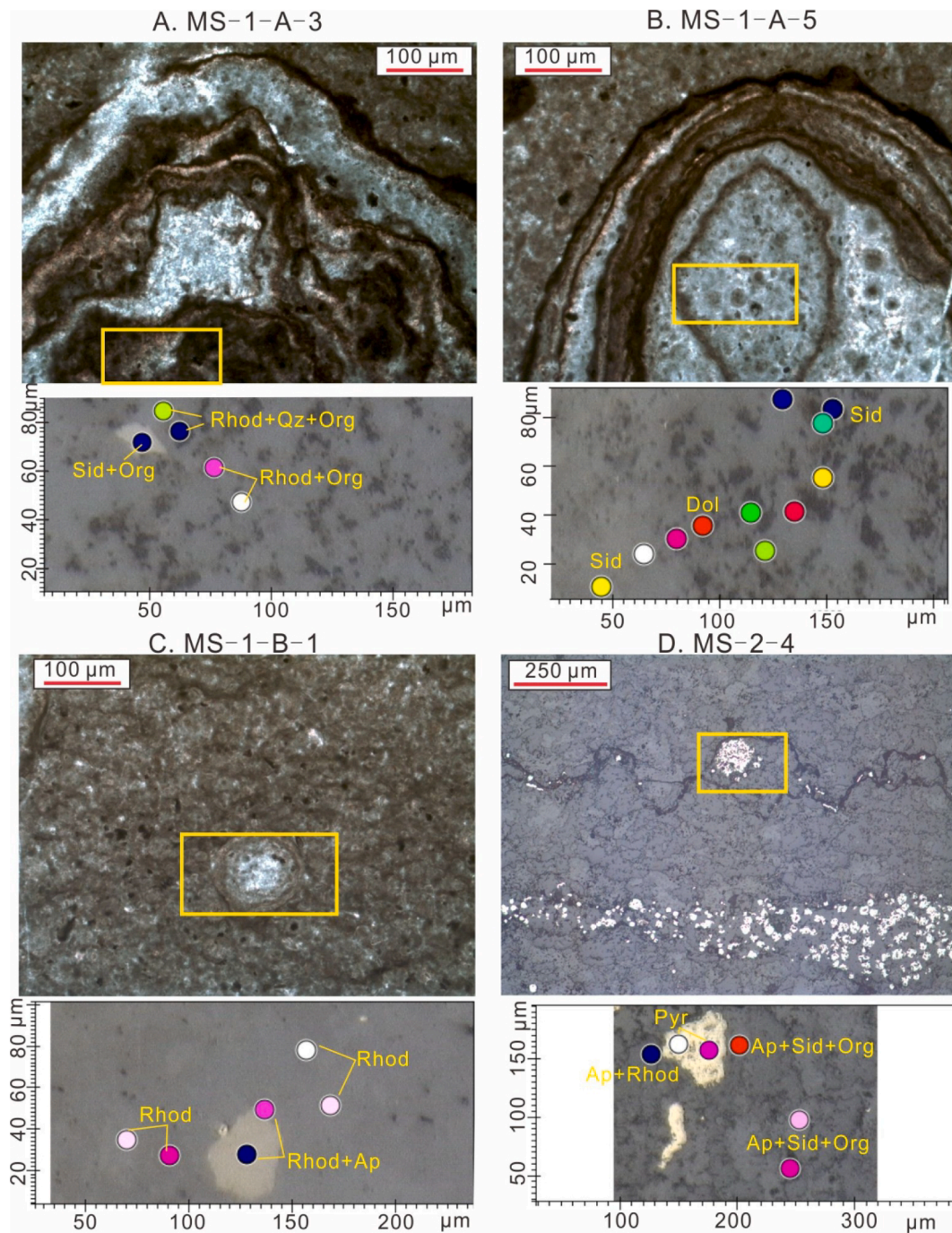


Fig. 9. Optical observation (upper) and analyzed points of Fourier transform infrared (FTIR) spectrometer (lower), yellow rectangles in optical photos show the same field of view in FTIR photos, colored dots in FTIR photos indicate the analyzed points. Please see results in [Supplementary materials](#). For abbreviation: Sid-siderite; Org-organic materials; Rhod- rhodochrosite; Dol-dolomite; Ap-apatite; Py-pyrite.

deposit of Úrkút in western Hungary preserved evidence of the Mn-metasomatism processes (Molnár et al., 2017). In that deposit, Mn oxides appeared with Fe oxides in laminated, micro-stromatolite-like structures that are explained as the results of syngenetic microbially-mediated mineralization of a feeder and mound system under the carbonate ore bed. In modern lakes, rhodochrosite nucleated on dissolving calcite crystals in the condition of high concentrations of dissolved Mn (>200 μM), forming primary Mn carbonate deposits (Herndon et al., 2018; Wittkop et al., 2020). Although both pathways could produce rhodochrosite, the portions of them during the formation of manganese deposits in the Baping Formation are uncertain. Mn-metasomatism required the Mn-bearing fluids infiltrating the unconsolidated micritic

marlstone and/or limestone, which may only be preserved in the margin of the calcite, as we observed in our samples, similarly to Molnár et al. (2017). For primary rhodochrosite formation, reported cases are limited to the freshwater of lacustrine environments (Herndon et al., 2018; Wittkop et al., 2020), which is contradictory to the marine environment of the Baping Formation.

6.1.2.3. Syngenetic Fe system. Fe-rich biomat formation intermingling with Mn-bearing carbonate layers (representing by sample MS-1A) of the Baping Formation offer an opportunity to define the environmental conditions. There are various types of microbial metabolisms that can oxidize Fe^{2+} in nature (Canfield et al., 2005). Three types of Fe-rich

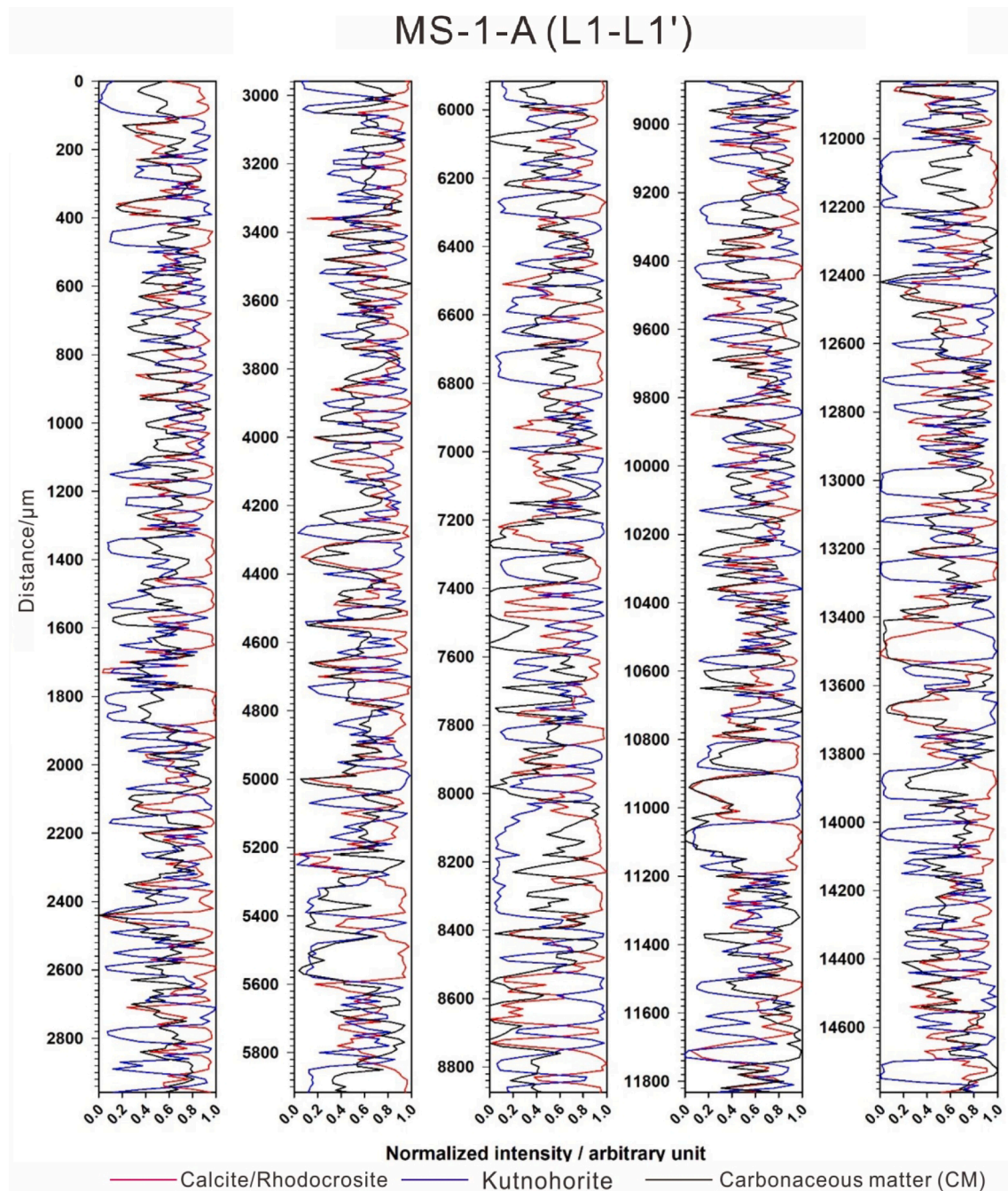


Fig. 10. Mineralogical and organic matter distribution in the Raman profile of sample MS-1-A (scan path is along L1-L1' in Fig. 4C).

biomats are considered for the Mn deposit of the Baping Formation, all of which are neutrophilic and consistent with basin conditions: (1) Microbial neutrophilic, micro-aerobic Fe(II) oxidizing bacteria (pH ~ 8; Eh + 0.3 V) (Hallbeck and Pedersen, 1990; Ehrenreich and Widdel, 1994; Konhauser, 1998; Ehrlich et al., 2015) supported by mineral assemblage (ferrihydrite, lepidocrosite, goethite, hematite); (2) Nitrate-reducing Fe (II) oxidizers in suboxic/anaerobic conditions without filaments (Straub et al., 1996); and (3) Photoferrotroph metabolism in anoxic/anaerobic light-demanding conditions, which is not plausible based on mineral assemblage, which supports suboxic-oxic conditions.

6.1.2.4. Diagenetic minerals. When microbes are alive, metals are sequestered in the extracellular polymeric substance (EPS) as cations on carboxyl, sulphidic acid, phosphate groups or/and anions on amino

groups. During the burial and early diagenesis stages, the EPS is degraded, and centers of metals/metalloids incorporated in organic matter can form (Dupraz and Visscher, 2005; Dupraz et al., 2009; Sforza et al., 2014). The nature of the local environment will have a fundamental influence on metal speciation.

6.1.2.5. Diagenetic Mn system. During diagenesis, the stabilization of the syngenetic Mn oxide and hydroxides proceeded, precipitating in pure forms (e.g. pyrolusite) and variable-cation-bound forms (e.g., Na, K, Ca, Mg, Ba, Fe, Ti) such as cryptomelane, jacobsonite, romanèchite, manjioreite and pyrophanite grew (Mandernack et al., 1995; Villalobos et al., 2003; Bargar et al., 2005; Bodeř et al., 2007; Johnson et al., 2016). Rhodocrosite can result from the activity of heterotrophic microbes during early diagenesis (Polgáři et al., 2012b; Maynard, 2014; Johnson

MS-2-long (L4-L4')

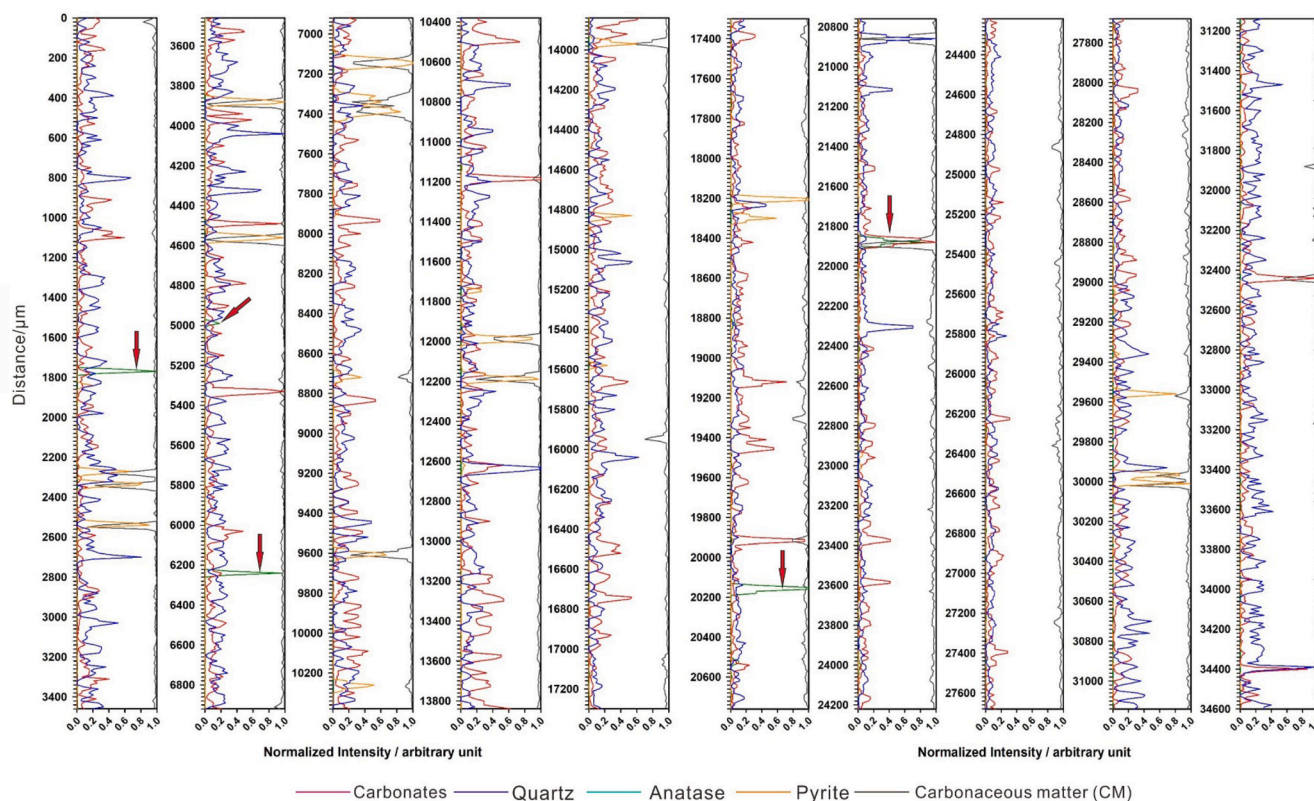


Fig. 11. Mineralogical and organic matter distribution in the Raman profile of sample MS-2 (scan path is along L4-L4' in Fig. 4E). Red arrows highlight anatase.

et al., 2016). These poorly mineralized cryptocrystalline mineral phases mixed in a variable amounts into the microlaminae as a manifestation of mineralized Mn cycles. In sample MS-1A, Mn-bearing carbonates are main ore minerals, while rhodochrosite and kutnohorite are considered diagenetic products (Fig. 13). Reaching the sulfate reduction zone (SRZ) in excess of organic matter, the contact zone mixing between Mn-oxide and SRZ resulted in the formation of MnS minerals (rambergite and alabandite), and kutnohorite (Aller and Rude, 1988; Burke and Kemp, 2002). In this contact zone high *in situ* H₂S and alkalinity concentrations are present below the Mn-oxide lamina. Large amounts of Mn²⁺ can be produced rapidly by bacterial Mn reduction of the Mn-oxide lamina; that is why large concentrations of Mn²⁺ occur at the sediment–water interface. The likely site of Mn-sulfide precipitation is therefore at the base of the Mn-oxide lamina, where high Mn²⁺ is met by high concentrations of H₂S diffusing upward. The precipitation of Mn-sulfide in preference to Mn-carbonate requires a high excess of free sulfide relative to alkalinity and an environment completely depleted in Fe, which would otherwise preferentially react with sulfide to form Fe-sulfides (Böttcher and Huckriede, 1997). High benthic Mn²⁺ concentrations in combination with high benthic carbonate alkalinity, produced *in situ* by bacterial sulfate reduction, can lead to supersaturation with respect to a mixed Mn-Ca-carbonate phase and to the formation of kutnohorite (Huckriede and Meischner, 1996).

6.1.2.6. Diagenetic Fe system. According to the diagenesis of Fe-rich biomats, the microbes produce poorly ordered ferrihydrite (lepidocrocite) as a primary mineral, which transforms to more ordered minerals, such as goethite or hematite and anatase (Fe-anatase, Fitzpatrick et al., 1978), within a few months or years via dissolution-dehydration processes (Konhauser, 1998; Schwertmann and Cornell, 2000; Kryc et al., 2003; Gyollai et al., 2015).

In an Fe-poor system one possibility for the Fe biomat to uptake Fe³⁺

may be the authigenic anatase (a Fe³⁺ Ti⁴⁺-bearing oxide), or anatase crystal structure (determined by Raman) (Fitzpatrick et al., 1978). Similarly to Glamoclija et al. (2009), we present here cyclic occurrence of anatase proposed as a mineralized microbial cycle (Fig. S3), which supports the scenario, that it is an example of microbial preservation in the form of anatase (TiO₂) permineralized microbial forms. So, as a first proposal in Mn carbonate ore formation, anatase represents mineralized Fe-biomats. The Fe reduction zone (FeRZ) is represented by siderite and ankerite occurrence. In the SRZ, pyrite also occurs, reflecting that locally anoxic conditions existed but did not become dominant. In the case of MS-2, pyrite laminae also occur. Amorphous silica segregation is derived by either the destruction of organic complexes or the transformation of ferrihydrite (Baele et al., 2008).

6.1.2.7. Combined diagenesis of the two ore-forming microbial systems. The segregated Si formed quartz cycles. The high silica content probably influenced the silica uptake of variable Mn oxide-hydroxide minerals. Through stabilization caused by diagenetic processes, the Mn oxide hydroxide bound not only Fe²⁺ and Fe³⁺ (e.g., jacobsonite, hollandite minerals), but also silica (braunite, serandite), to form a highly variable content of oxide-silicate mixed minerals. These are characterized by highly variable composition. Texturally, mineral habits are strongly modulated (and perhaps templated) by extracellular polymeric substances that form a network of pore spaces.

Braunite is a trace occurrence in the analyzed samples. The interpretation is that braunite formation is due to combined diagenesis, as the segregated silica needed for braunite is typical of Fe- or cyanobacterial system diagenesis. The most likely formation of braunite is sedimentary or early diagenetic via biogeochemically mediated processes, as proposed by Johnson et al. (2016) and Biondi et al. (2020). These studies report scenarios that are broadly similar to our MS-1 samples. While syngenetic mineralization took place under oxic neutrophilic conditions,

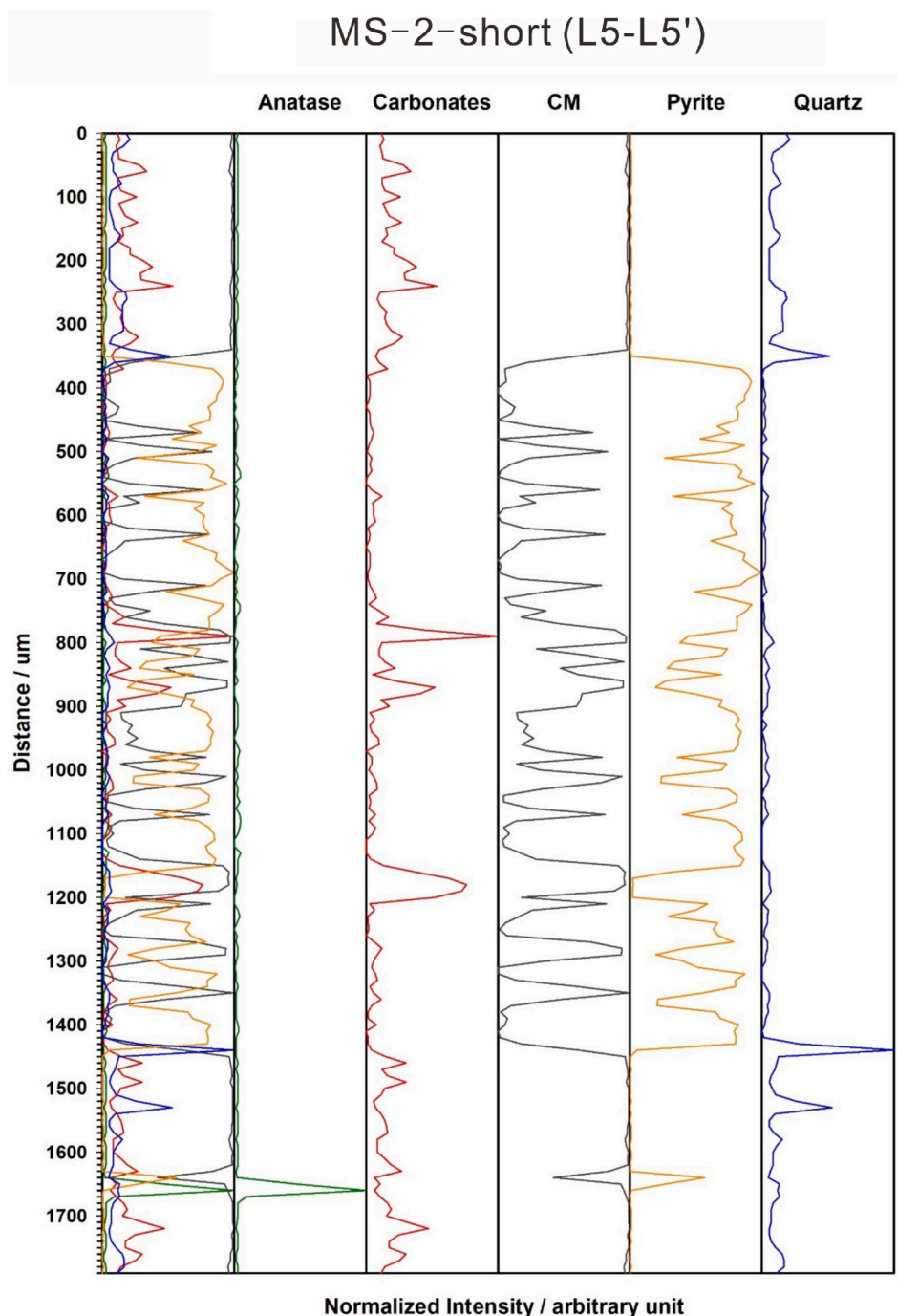


Fig. 12. Mineralogical distribution in the Raman profile of sample MS-2 (scan path is along L5-L5' in Fig. 4E).

slightly alkaline and oxic conditions were also reported for braunite formation (pH 9.5–9.9; Eh + 0.43 V; Listova, 1961); this fits well with our scenario.

Serandite traces, as an oxide-silicate mineral, also belong to this process (empirical composition of hollandite also can contain Si). Jacobsite can be interpreted as the transitional form between Mn and Fe oxides.

6.1.2.8. Diagenesis of other minerals. After death and decomposition of cells, as well as breakdown of EPS, ions that were previously bound on their surfaces release Ca, Mg, Na, K, Ti, P, S, Si, Co, Zn, Ba, Sr, and rare earth elements. These are bioactive elements, as stated in previous studies (Kryc et al., 2003; Meyer et al., 2012; Gyollai et al., 2017; Yu

et al., 2019; Biondi et al., 2020). Formation of CO_3^{2-} , PO_4^{3-} , SiO_4^{4-} , and SO_4^{2-} anions commences and a complex transforming mineralization begins to take place, which (depending on local geochemical conditions) can result in clay minerals, mixed carbonates, feldspar, silica, and apatite. These poorly crystallized minerals can transform into more stable minerals over time (Konhauser, 1998; Dupraz and Visscher, 2005). The various geochemical features of Mn ores are modulated by such syngenetic and diagenetic processes. These include increased Co content compared with crustal abundance, a characteristic feature for Urucum ores as well as the Úrkút locality (Polgári et al., 2012b; Biondi and Lopez, 2017). Reaction of Fe oxidation bacteria with Co proceeds easily, and Mn oxidation bacteria can also oxidize cobalt and REE (Ce) (Moffett, 1994; Loges et al., 2012). In the Carboniferous Longtou

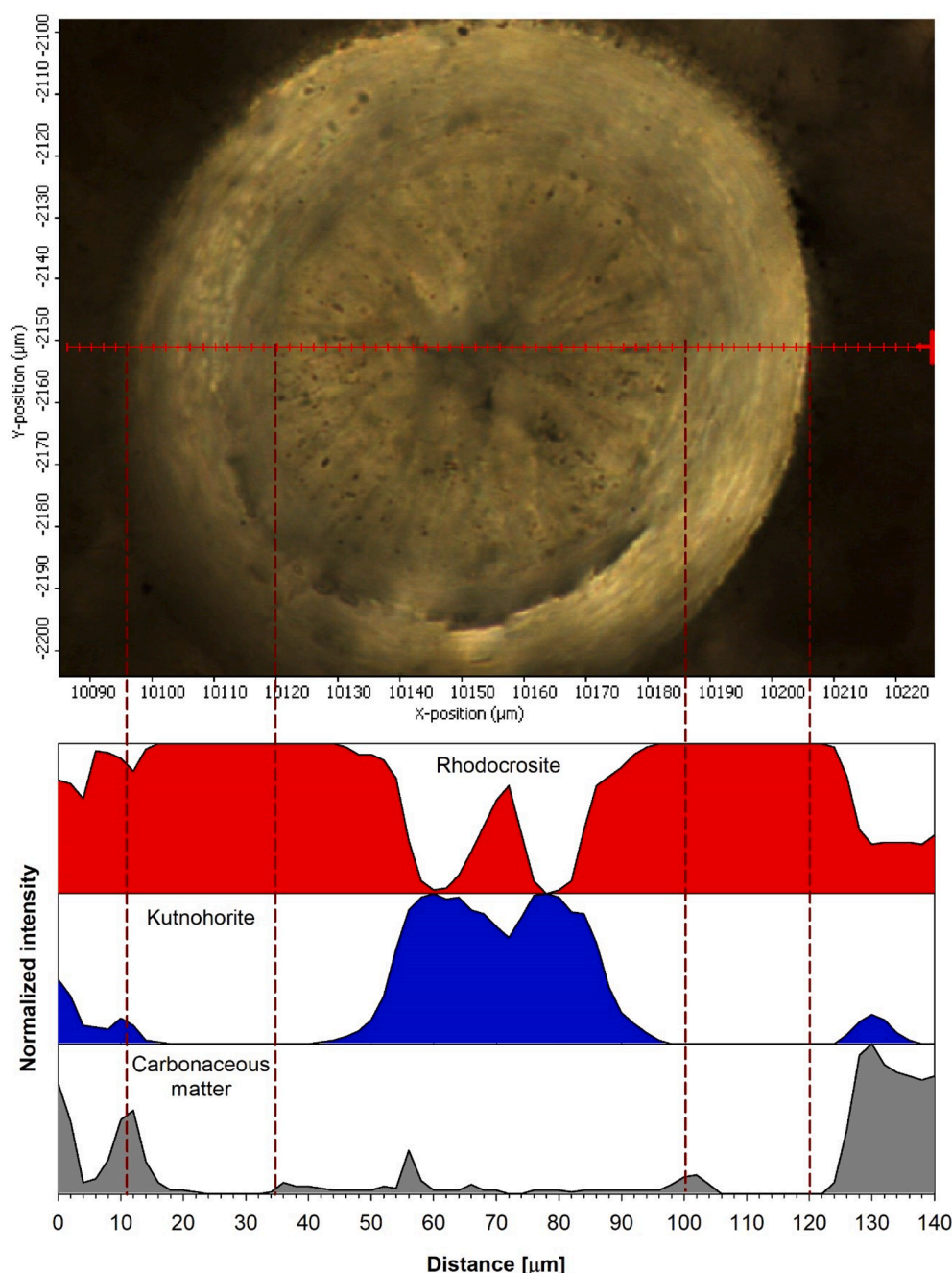


Fig. 13. Mineralogical and organic matter distribution in the Raman profile of a nodule in sample MS-1.

manganese deposit, MnO contents of Mn-ore range from 6.81% to 32.3% (average = 17.34%). The trace element contents, among them Sr, Li, Co, Ni, Zn, Mo, Ba, W, Ti, and U, are relatively enriched in the Mn-ore, and are significantly higher than average crustal abundances (Wu et al., 2016; Yu et al., 2016). The liberation of the cell surface-bound elements provided sources of these elements (Polgári et al., 2019).

The amorphous silica can easily transform into more stable minerals such as quartz (Herdianita et al., 2000; Campbell et al., 2001). Abundant quartz in MS-2 is common and forms cycles. Feldspar and montmorillonite traces occur. Montmorillonite traces are formed by the leaching of biofilm alkali elements (Na, K, Al, Mg) (Gyollai et al., 2015, 2017). Clay mineral formation did not become considerable. Apatite can precipitate at pH of 7–8 and occurs in micrometer-sized crystals; similar apatite occurrences were noted in our samples, based on Raman and CL analyses. Among carbonates, the dolomite (ankerite) is present but scarce.

Barite and johannite belong to the sulfates that form from marine sulfate and/or organic constituents. Barite, a mineral precipitating under typical oxic conditions ($E_h > +0.2$) at low temperature, is considered here as oxygen supply indicator, because barite occurring with hematite indicates conditions that are more oxic than when occurring without hematite (Hanor, 2000). Occurrence of Na-jarosite refers to local anoxic diagenetic conditions.

Considering the mineral assemblage, it is clear that the initially highly segregated silica content did not support clay formation via early diagenesis, and silica-consuming minerals are numerous, which finally resulted in a decrease in silica content, which decreased quartz formation. Authigenic formation of these minerals is also common in microbially-mediated diagenetic processes, and these minerals are non-luminescent (Marshall 1998; Hassouta et al. 1999).

Most of the minerals detected here have well characterized

formation conditions, as summarized in Table S5. Based on mineralogy, proto-ore sedimentation and diagenesis occurred under suboxic-obligatory to oxic and semi-neutral to alkaline conditions. During diagenesis in excess of organic matter, sulfate reduction under anoxic/anaerobic conditions also became significant.

6.2. Metallogenic model based on high resolution mineralogical study

Complex microbial lamination in the Early Carboniferous manganese deposits of central Guangxi is supported by the cross validation of different analyses on the representative thin sections. Cyanobacteria, Mn bacteria and Fe bacteria jointly controlled the formation of the manganese deposits, and the metallogenic model can be divided into two main stages.

6.2.1. Sediment accumulation

The sediment surface in the basin was densely colonized by cyanobacteria (OM, mineralized microbially produced structure). Detritus contribution was scarce, indicating that the basin was starved in the sense of detritus contribution during the Mn ore deposition. Marine current activity resulted in obligatory oxic conditions, and distal hydrothermal fluids contributed to the chemical nutrient Mn(II) supply. Enzymatic Mn(II) oxidation resulted in δMnO_2 biooxide (todorokite, manganite) accumulation as very fine grained ooze in the cyanobacterial organic and carbonate network. This process sequestered Mn(II) from solution to solid phase. Intense carbonate formation by cyanobacterial activity is also proposed on optical microscopy, and it was affected by Mn metasomatism. A considerable amount of microbial organic matter was accumulated. The cyanobacterial activity lead to the enrichment of bioessential elements (e.g., Ca, Si, P, and others) in the system, binding these elements and silica on EPS. When EPS is degraded, centers of metals/metalloids incorporated in organic matter can form. The nature of the local environment will have a fundamental influence on metal speciation. As in any element cycle, decoupling of reductive and oxidative processes would increase either the oxidized or reduced reservoir (Dupraz and Visscher, 2005; Dupraz et al., 2009; Sforza et al., 2014). The cyanobacteria have growth cyclicity (probably a daily cycle) and Mn-oxidizing microbes have their own, and these two cycles co-existed in one space. Occasional activities of Fe(II) oxidizing microbes and their weak biomats are represented by particular minerals (ferrihydrite, lepidocrocite).

It is supposed that cyanobacterial activity produced and supplied oxygen into the system as “microbial ventilation” via photosynthesis, as proposed by Yu et al. (2019). The accumulation in this case happened in the photic zone. Mn(II) oxidation cycles consumed oxygen content regularly. The alternating lamination of the Mn-bearing carbonate minerals (calcite/rhodochrosite and kutnohorite) represents cyanobacterial carbonate and Mn-microbial cycles, while quartz laminations shown in the Raman profiles also probably represent cyanobacterial cycles.

6.2.2. After burial – Early and later diagenesis

During early and later diagenesis, the fate of cyanobacterial and Mn microbial activity and also Fe microbial activity was combined, and the conditions turned suboxic than anoxic (mostly like in SRZ), which is proved by framboidal pyrite in the samples. Contact between SRZ and Mn oxide/MnRZ or SRZ contact with discharging Mn^{2+} formed rambergite, alabandite, and kutnohorite (MnS-kutnohorite formation model, Burke and Kemp, 2002). During diagenesis variable mineral assemblage formed (Table S5).

Mn-metasomatism of cyanobacterial carbonate formed Mn-bearing calcite. Syngenetic δMnO_2 bio-oxide via degradation of organic matter in microbially-mediated process resulted in the formation of Ca-rhodochrosite (negative $\delta^{13}\text{C}$ signal, Liu, 1990; Chen et al., 2008; Yu et al., 2017), which is the main process of formation of early diagenetic rhodochrosite ore (Roy, 2006; Maynard, 2014). At the same time,

decomposition of cyanobacterial cells and EPS started, which led to the liberation of Ca^{2+} , silica, P, and other elements (K, Al, Ti, etc.). The system is in excess of Ca^{2+} , which attracted the earlier formed rhodochrosite and substitutes a part of manganese forming Mn-bearing calcite (Herdon et al., 2018) and also kutnohorite. The formation of kutnohorite is probably supported by elevated temperature and the strong effect of organic matter (Burke and Kemp, 2002).

Living cyanobacteria adhere silica on their surface (Dupraz and Visscher, 2005), and after death of cells, silica liberalizes to form quartz, which occurs as fine cyclic quartz laminae. P and Ca^{2+} formed apatite (fine-grained phosphorite and further forming larger size minerals); their distributions are well shown in CL photos (Fig. 6). Although it is convenient to explain feldspar as the detritus material, based on FTIR and EPMA-EDS results it is most probably diagenetic, for the size of the feldspar is very fine and uniform, which is similar to the carbonate minerals. The EPS network via diagenesis kept the space until the diagenetic mineral formation took place (Yu et al., 2019; Biondi et al., 2020).

The system reached anoxic conditions and triggered the sulfate reduction; pyrite, rambergite, and alabandite were formed during diagenesis. Fe biomat diagenesis resulted in anatase (Fe-anatase) cycles. Clay mineralization did not become dominant. In this stage, syngenetic clay mineralization did not occur (or was not dominant), this feature is similar to the manganese ore deposit in the Datangpo Formation (Yu et al., 2019). We propose two potential explanations for the absence of the clay minerals: (1) the manganese ore deposits formed in the distal position of the basin, thus the terrigenous detritus could not reach this area; (2) Formation of the diagenetic clay minerals was suppressed, which is probably linked to the following scenarios: (i) the liberalization of ions was not synchronous, since if Ca liberalized first, it could incorporate to carbonates, and later liberalizing silica could form quartz, (ii) if the silica liberalized first, the other ions were missing for clay formation, so it formed quartz, (iii) the conditions were not favorable for clay mineral formation.

7. Conclusions

Microscopic observation, mineralogical, geochemical and isotopic analyses demonstrate that the manganese deposits of the Early Carboniferous Baping Formation in the Youjiang Basin of the central Guangxi, South China preserved the evidence of microbial metallogenesis. Represented samples of Mn-bearing carbonate (MS-1, $\text{MnO} \leq 10\%$) and Mn ore (MS-2, $\text{MnO} > 10\%$) show massive and laminated structure, respectively, and both samples contain petrographic evidence of disseminated mineralized microbial biosignatures in microscopic scale. Mn-bearing carbonate records positive $\delta^{13}\text{C}$ value (+1.53‰), whereas Mn ores have negative $\delta^{13}\text{C}$ value (−7.15‰ to −3.64‰), indicating that the participation of organic carbon influenced the carbon isotopic system in the manganese deposit. Detailed *in situ* mineralogical study in microscale based on CL, FTIR, SEM-EDS, and Raman spectroscopy further identifies the syngenetic and diagenetic Mn and Fe systems during the formation of the manganese deposit, both of which were formed by biomats and precipitated micro-laminae of microbiogenic minerals such as Mn-calcite, rhodochrosite, kutnohorite, and apatite. The metallogenic model can be divided into two main stages. During the sediment accumulation stage, enzymatic Mn(II) oxidation controlled the accumulation of Mn oxides within the cyanobacterial organic and carbonate network, leading to the enrichment of the manganese. During the stages of diagenesis, Mn-metasomatism of cyanobacterial carbonate and the reaction between syngenetic manganese oxides and the organic matters led to the precipitation of proto-ore (Ca-rhodochrosite). The occurrence of kutnohorite is probably linked with the transition of Mn-sulfide, while anatase represents the diagenesis of Fe-bioma. After the release of elements in the decomposed cells and EPS, a series of accessory minerals (feldspar, apatite, pyrite, etc.) formed.

Declaration of Competing Interest

The authors declare that they have no known competing financial interests or personal relationships that could have appeared to influence the work reported in this paper.

Acknowledgments

This study was supported by the Natural Science Foundation of China (No. U1812402 and No. 42072131), the prospecting project of the Department of Natural Resources of Guangxi Zhuang Autonomous Region (No. 2020-1124). The authors are also grateful for the support of the National Research, Development and Innovation Office (Hungary), National Scientific Research Fund No. 125060. The comments of anonymous reviewers are highly appreciated.

Appendix A. Supplementary data

Supplementary data to this article can be found online at <https://doi.org/10.1016/j.oregeorev.2021.104251>.

References

- Aller, R.C., Rude, P.D., 1988. Complete oxidation of solid phase sulfides by manganese and bacteria in anoxic marine sediments. *Geochim. Cosmochim. Acta* 52 (3), 751–765.
- Baele, J.-M., Boulvain, F., De Jong, J., Matielli, N., Papier, S., Pr  at, A., 2008. Iron microbial mats in Modern and Phanerozoic environments. *Proc. SPIE* 7097.
- Baioumy, H.M., Khedr, M.Z., Ahmed, A.H., 2013. Mineralogy, geochemistry and origin of Mn in the high-Mn iron ores, Bahariya Oasis. *Egypt. Ore Geol. Rev.* 53, 63–76.
- Bargar, J.R., Tebo, B.M., Bergmann, U., Webb, S.M., Glatzel, P., Chiu, V.Q., Villalobos, M., 2005. Biotic and abiotic products of Mn (II) oxidation by spores of the marine *Bacillus* sp. strain SG-1. *Am. Min.* 90 (1), 143–154.
- Beasley, M.M., Bartelink, E.J., Taylor, L., Miller, R.M., 2014. Comparison of transmission FTIR, ATR, and DRIFT spectra: implications for assessment of bone bioapatite diagenesis. *J. Archaeol. Sci.* 46, 16–22.
- BGMRGZAR, 1985. Regional Geology of Guangxi Zhuang Autonomous Region. Geological Published House, Beijing.
- Biondi, J.C., Polg  ri, M., Gyollai, I., Fintor, K., Kov  cs, I., Fekete, J., Mojzsis, S.J., 2020. Biogenesis of the neoproterozoic kremyidilite manganese ores from urucum (brazil) – A new manganese ore type. *Precamb. Res.* 340, 105624. <https://doi.org/10.1016/j.precamres.2020.105624>.
- Biondi, J.C., Lopez, M., 2017. Urucum Neoproterozoic-Cambrian manganese deposits (MS, Brazil): Biogenic participation in the ore genesis, geology, geochemistry, and depositional environment. *Ore Geol. Rev.* 91, 335–386.
- Bodei, S., Manceau, A., Geoffroy, N., Baronn  t, A., Buatier, M., 2007. Formation of todorokite from vernadite in Ni-rich hemipelagic sediments. *Geochim. Cosmochim. Acta* 71 (23), 5698–5716.
- B  ttcher, M.E., Huckriede, H., 1997. First occurrence and stable isotope composition of authigenic γ -MnS in the central Gotland Deep (Baltic Sea). *Marine Geology* 137, 201–205.
- Burke, I.T., Kemp, A.E.S., 2002. Microfabric analysis of Mn-carbonate laminae deposition and Mn-sulfide formation in the Gotland Deep, Baltic Sea. *Geochim. Cosmochim. Acta* 66 (9), 1589–1600.
- Calvert, S.E., Pedersen, T.F., 1996. Sedimentary geochemistry of manganese; implications for the environment of formation of manganiferous black shales. *Economic Geology* 91, 36–47.
- Campbell, K.A., Sannazzaro, K., Rodgers, K.A., Herdianita, N.R., Browne, P.R.L., 2001. Sedimentary Facies and Mineralogy of the Late Pleistocene Umukuri Silica Sinter, Taupo Volcanic Zone, New Zealand. *J. Sediment. Res.* 71 (5), 727–746.
- Canfield, D.E., Erik, K., Bo, T., 2005. The Iron and Manganese Cycles. In: Canfield, D.E., Kristensen, E., Thamdrup, B. (Eds.), *Adv. Mar. Biol.* Academic Press, pp. 269–312.
- Chan, C.S., Fakra, S.C., Emerson, D., Fleming, E.J., Edwards, K.J., 2011. Lithotrophic iron-oxidizing bacteria produce organic stalks to control mineral growth: implications for biosignature formation. *ISME J.* 5 (4), 717–727.
- Chen, F., Qingfei, W., Yang, S., Zhang, Q., Liu, X., Chen, J., Carranza, E.J., 2018. Space-time distribution of manganese ore deposits along the southern margin of the South China Block, in the context of Palaeo-Tethyan evolution.
- Chen, J.-Y., Schopf, J.W., Bottjer, D.J., Zhang, C.-Y., Kudryavtsev, A.B., Tripathi, A.B., Wang, X.-Q., Yang, Y.-H., Gao, X., Yang, Y., 2007. Raman spectra of a Lower Cambrian ctenophore embryo from southwestern Shaanxi, China. *Proc. Natl. Acad. Sci. USA* 104 (15), 6289–6292.
- Chen, X., Jiang, S., 2018. Discovery of the largest Carboniferous manganese deposit in Longtuo-Limiao, central Guangxi, China. *China Geol.* 1, 312–313.
- Chen, X.-i., Li, D.-a., Ling, H.-F., Jiang, S.-Y., 2008. Carbon and sulfur isotopic compositions of basal Datangpo Formation, northeastern Guizhou, South China: Implications for depositional environment. *Progr. Nat. Sci.* 18 (4), 421–429.
- Das, S., Hendry, M.J., 2011. Application of Raman spectroscopy to identify iron minerals commonly found in mine wastes. *Chem. Geol.* 290 (3–4), 101–108.
- Dupraz, C., Reid, R.P., Braissant, O., Decho, A.W., Norman, R.S., Visscher, P.T., 2009. Processes of carbonate precipitation in modern microbial mats. *Earth Sci. Rev.* 96 (3), 141–162.
- Dupraz, C., Visscher, P.T., 2005. Microbial lithification in marine stromatolites and hypersaline mats. *Trends Microbiol.* 13 (9), 429–438.
- Ehrenreich, A., Widdel, F., 1994. Anaerobic oxidation of ferrous iron by purple bacteria, a new type of phototrophic metabolism. *Appl. Environ. Microbiol.* 60, 4517–4526.
- Ehrlich, H.L., Newman, D.K., Kappler, A., 2015. Ehrlich's geomicrobiology. CRC Press.
- Ewers, W.E., 1983. Chapter 13 Chemical Factors in the Deposition and Diagenesis of Banded Iron-Formation. In: Trendall, A.F., Morris, R.C. (Eds.), *Developments in Precambrian Geology*. Elsevier, pp. 491–512.
- Fan, D., Yang, P., 1999. Introduction to and classification of manganese deposits of China. *Ore Geol. Rev.* 15 (1–3), 1–13.
- Fan, D., Ye, J., Yin, L., Zhang, R., 1999. Microbial processes in the formation of the Sinian Gaoyan manganese carbonate ore, Sichuan Province, China. *Ore Geol. Rev.* 15 (1–3), 79–93.
- Fernandez, J.R.L., Souza-Parise, M.d., Morais, P.C., 2015. Structural characterization and simulation of colloidal MnS. *Mater. Res. Express* 2 (9), 095019. <https://doi.org/10.1088/2053-1591/2/9/095019>.
- Fischer, W.W., Hemp, J., Johnson, J.E., 2015. Manganese and the evolution of photosynthesis. *Origins Life Evol. Biospheres* 45 (3), 351–357.
- Fitzpatrick, R., Roux, J., Schwertmann, U., 1978. Amorphous and crystalline titanium and iron-titanium oxides in synthetic preparations, at near ambient conditions, and in soil clays. *Clays Clay Miner.* 26, 189–201.
- Force, E.R., Cannon, W.F., 1988. Depositional model for shallow-marine manganese deposits around black shale basins. *Economic Geology* 83, 93–117.
- Frost, R.L., Erickson, K.L.,   jka, J., Reddy, B.J., 2005. A Raman spectroscopic study of the uranyl sulphate mineral johannite. *Spectrochim. Acta Part A Mol. Biomol. Spectrosc.* 61 (11–12), 2702–2707.
- Glamoclija, M., Steele, A., Fries, M., Schieber, J., Voytek, M.A., Cockell, C.S., 2009. Association of anatase (TiO₂) and microbes: Unusual fossilization effect or a potential biosignature? *Geol. Soc. Am. Special Papers*. [https://doi.org/10.1130/2009.2458\(42\)](https://doi.org/10.1130/2009.2458(42)), Geological Society of America Special Papers 2009;458;965–975.
- Glasby, G.P., 1988. Manganese deposition through geological time: dominance of the post-eocene deep-sea environment. *Ore Geol. Rev.* 4 (1–2), 135–143.
- Glotch, T.D., Rossman, G.R., 2009. Mid-infrared reflectance spectra and optical constants of six iron oxide/oxyhydroxide phases. *Icar* 204 (2), 663–671.
- Gracheva, M., Homonnay, Z., Kov  cs, K., Kende Attila B  res, K.A., Biondi, J.C., Yu, W., Kov  cs Kis, V., Gyollai, I., Polg  ri, M., 2021. M  ssbauer characterization of microbially mediated iron and manganese ores of variable geological ages. Submitted to current volume.
- Gyollai, I., Polg  ri, M., Fintor, K., P  l-Moln  r, E., Popp, F., Koeberl, C., 2017. Microbial activity records in Marinoan Snowball Earth postglacial transition layers connecting diamicite with cap carbonate (Otavi Group, NW-Namibia). *Austrian J. Earth Sci.* 110 (1) <https://doi.org/10.17738/ajes10.17738/ajes.2017.0001>.
- Gyollai, I., Polg  ri, M., Fintor, K., Popp, F., Mader, D., P  l-Moln  r, E., Nagy, S., Koeberl, C., 2015. Microbially mediated deposition of postglacial transition layers from the neoproterozoic otavi group, Namibia: Evidence of rapid deglaciation after the sturtian cryogenic period. *Carpathian J. Earth Environ. Sci.* 10, 63–76.
- Hallbeck, L., Pedersen, K., 1990. Culture parameters regulating stalk formation and growth rate of *Gallionella ferruginea*. *Microbiol.* 136 (9), 1675–1680.
- Hanor, J.S., 2000. Barite–Celestine Geochemistry and Environments of Formation. *Reviews in Mineralogy and Geochemistry* 40, 193–275.
- Hassouta, L., Buatier, M.D., Potdevin, J.L., Liewig, N., 1999. Clay diagenesis in the sandstone reservoir of the Ellon field (Alwyn, North Sea). *Clays Clay Miner.* 47, 269–285.
- Herdianita, N.R., Browne, P.R.L., Rodgers, K.A., Campbell, K.A., 2000. Mineralogical and textural changes accompanying ageing of silica sinter. *Miner. Deposita* 35 (1), 48–62.
- Herndon, E.M., Havig, J.R., Singer, D.M., McCormick, M.L., Kump, L.R., 2018. Manganese and iron geochemistry in sediments underlying the redox-stratified Fayetteville Green Lake. *Geochim. Cosmochim. Acta* 231, 50–63.
- Huang, H.-u., Du, Y.S., Huang, Z.Q., Yang, J.H., Huang, H.W., Xie, C.X., Hu, L.S., 2013. Depositional chemistry of chert during late Paleozoic from western Guangxi and its implication for the tectonic evolution of the Youjiang Basin. *Sci. China: Earth Sci.* 56 (3), 479–493.
- Huang, H., Yan, J.X., Yu, W.C., 2020. Evolution of Yizhou aulacogen in Guangxi during Late Paleozoic and distribution of manganese deposits in Early Carboniferous. *J. Palaeogeogr. (Chinese Edition)* 22, 1001–1011 (In Chinese with English abstract).
- Huckriede, H., Meischner, D., 1996. Origin and environment of manganese-rich sediments within black shale basins. *Geochim. Cosmochim. Acta* 60 (8), 1399–1413.
- Jehli  ka, J., Vitek, P., Edwards, H.G.M., 2009. Fast nondestructive Raman spectroscopic detection of minerals and biomolecules for exobiological studies. *Geochimica Et Cosmochimica Acta* 73.
- Johnson, J.E., Webb, S.M., Ma, C., Fischer, W.W., 2016. Manganese mineralogy and diagenesis in the sedimentary rock record. *Geochim. Cosmochim. Acta* 173, 210–231.
- Jones, S., McNaughton, N.J., Grguric, B., 2013. Structural controls and timing of fault-hosted manganese at Woodie Woodie, East Pilbara, Western Australia. *Ore Geol. Rev.* 50, 52–82.
- Julien, C.M., Massot, M., Poin  signon, C., 2004. Lattice vibrations of manganese oxides: Part I. Periodic structures. *Spectrochim. Acta Part A Mol. Biomol. Spectrosc.* 60 (3), 689–700.
- Konhauser, K.O., 1998. Diversity of bacterial iron mineralization. *Earth Sci. Rev.* 43 (3–4), 91–121.

- Kryc, K.A., Murray, R.W., Murray, D.W., 2003. Al-to-oxide and Ti-to-organic linkages in biogenic sediment: relationships to paleo-export production and bulk Al/Ti. *Earth Planet. Sci. Lett.* 211 (1–2), 125–141.
- Lafuente, B., Downs, R.T., Yang, H., Stone, N., 2016. The power of databases. In: Armbruster, T., Danisi, R.M. (Eds.), *The RRUFF project*. Walter de Gruyter GmbH, Berlin, Germany, W. De Gruyter, pp. 1–29.
- Lin, H., Szeinbaum, N.H., DiChristina, T.J., Taillefer, M., 2012. Microbial Mn(IV) reduction requires an initial one-electron reductive solubilization step. *Geochim. Cosmochim. Acta* 99, 179–192.
- Liu, T., 1990. C-S relationships in shales hosting manganese ores from Mexico, China, and Newfoundland: Implications for depositional environment and mineralization. *Ore Geol. Rev.* 5 (4), 325–340.
- Listov, L.P., 1961. Experimental studies of physico-chemical conditions of sedimentation of manganese oxides and carbonate. *Ocherki Metallogen. Osadochn. Porod. Publication of the AN USSR, Moscow*, pp. 319–351.
- Loges, A., Wagner, T., Barth, M., Bau, M., Göb, S., Markl, G., 2012. Negative Ce anomalies in Mn oxides: The role of Ce⁴⁺ mobility during water–mineral interaction. *Geochim. Cosmochim. Acta* 86, 296–317.
- Lovley, D.R., 1991. Dissimilatory Fe(III) and Mn(IV) reduction. *Microbiol. Rev.* 55, 259–287.
- Madecová, J., Komádel, P., 2001. Baseline Studies of the Clay Minerals Society Source Clays: Infrared Methods.
- Mandernack, K.W., Post, J., Tebo, B.M., 1995. Manganese mineral formation by bacterial spores of the marine bacillus, Strain SG-1: Evidence for the direct oxidation of Mn (II) to Mn (IV). *Geochim. Cosmochim. Acta* 59 (21), 4393–4408.
- Marshall, D.J., 1998. Cathodoluminescence of Geological Materials. Unwin Hyman, Boston, p. 146.
- Maynard, B., 2014. Manganiferous sediments, rocks, and ores. In: Holland, H.D., Turekian, K.K. (Eds.), *Treatise on Geochemistry*, 2nd edition. Pergamon, Oxford, pp. 289–308.
- Maynard, J.B., 2003. In: *Treatise on Geochemistry*. Elsevier, pp. 289–308. <https://doi.org/10.1016/B0-08-043751-6/07099-7>.
- Meyer, E.E., Quicksall, A.N., Landis, J.D., Link, P.K., Bostick, B.C., 2012. Trace and rare earth elemental investigation of a Sturtian cap carbonate, Pocatello, Idaho: Evidence for ocean redox conditions before and during carbonate deposition. *Precamb. Res.* 192–195, 89–106.
- Moffett, J.W., 1994. A radiotracer study of cerium and manganese uptake onto suspended particles in Chesapeake Bay. *Geochim. Cosmochim. Acta* 58 (2), 695–703.
- Molnár, Z., Polgári, M., Hein, J.R., Józsa, S., Fekete, J., Gyollai, I., Fintor, K., Bíró, L., Szabó, M., Rapi, S., Forgó, P., Vigh, T., 2017. Fe-Mn oxide indications in the feeder and mound zone of the Jurassic Mn-carbonate ore deposit, Úrkút, Hungary. *Ore Geol. Rev.* 86, 839–855.
- Müller, C.M., Pejčic, B., Esteban, L., Piane, C.D., Raven, M., Mizaikoff, B., 2014. Infrared Attenuated Total Reflectance Spectroscopy: An Innovative Strategy for Analyzing Mineral Components in Energy Relevant Systems. *Sci. Rep.* 4, 6764.
- Myers, C.R., Nealson, K.H., 1988. Bacterial manganese reduction and growth with manganese oxide as the sole electron acceptor. *Science* 240 (4857), 1319–1321.
- Nealson, K.H., Saffarini, D., 1994. Iron and manganese in anaerobic respiration: Environmental significance, physiology, and regulation. *Annu. Rev. Microbiol.* 48 (1), 311–343.
- Okolo, G.N., Neomagus, H.W.J.P., Everson, R.C., Roberts, M.J., Bunt, J.R., Sakurovs, R., Mathews, J.P., 2015. Chemical–structural properties of South African bituminous coals: Insights from wide angle XRD–carbon fraction analysis, ATR–FTIR, solid state ¹³C NMR, and HRTEM techniques. *Fuel* 158, 779–792.
- Orange, D., Knittle, E., Farber, D., Williams, Q., 1996. Raman spectroscopy of crude oils and hydrocarbon fluid inclusions: A feasibility study. In: Dyar, M.D., McCammon, C., Schaefer, M.W. (Eds.), *The Geochemical Society, 5. Special Publication*, pp. 65–81.
- Ostwald, J., 1981. Evidence for a biogeochemical origin of the Groote Eylandt manganese ores. *Economic Geology* 76, 556–567.
- Parikh, S.J., Chorover, J., 2006. ATR-FTIR spectroscopy reveals bond formation during bacterial adhesion to iron oxide. *Langmuir* 22 (20), 8492–8500.
- Polgári, M., Bajnóczi, B., Kovács, K., Götz, J., Dobosi, G., Tóth, M., Vigh, T., 2007. Mineralogical and cathodoluminescence characteristics of Ca-rich kutnohorite from the Úrkút Mn-carbonate mineralization, Hungary. *MinM* 71 (5), 493–508.
- Polgári, M., Gyollai, I., Fintor, K., Horváth, H., Elemér, P.-M., Biondi, J.C., 2019. Microbially mediated ore-forming processes and cell mineralization. *Front. Microbiol.* 10, 2731.
- Polgári, M., Hein, J., Tóth, A., Pál-Molnár, E., Vigh, T., Bíró, L., Fintor, K., 2012a. Microbial action formed Jurassic Mn-carbonate ore deposit in only a few hundred years (Úrkút, Hungary). *Geology* 40, 903–906.
- Polgári, M., Hein, J.R., Vigh, T., Szabó-Drubina, M., Fórizs, I., Bíró, L., Müller, A., Tóth, A.L., 2012b. Microbial processes and the origin of the Úrkút manganese deposit, Hungary. *Ore Geol. Rev.* 47, 87–109.
- Polgári, M., Hein, J.R., Bíró, L., Gyollai, I., Németh, T., Sajgó, C., Fekete, J., Schwark, L., Pál-Molnár, E., Hámor-Vidó, M., Vigh, T., 2016. Mineral and chemostratigraphy of a Toarcian black shale hosting Mn-carbonate microbialites (Úrkút, Hungary). *Palaeogeogr. Palaeoclimatol. Palaeoecol.* 459, 99–120.
- Rajabzadeh, M.A., Haddad, F., Polgári, M., Fintor, K., Walter, H., Molnár, Z., Gyollai, I., 2017. Investigation on the role of microorganisms in manganese mineralization from Abadeh-Tashk area, Fars Province, southwestern Iran by using petrographic and geochemical data. *Ore Geol. Rev.* 80, 229–249.
- Ru, T.Q., Wei, L.D., Shu, M., 1992. Manganese deposits in Guangxi. Geological Published House, Beijing (In Chinese).
- Roy, S., 2006. Sedimentary manganese metallogenesis in response to the evolution of the Earth system. *Earth Sci. Rev.* 77 (4), 273–305.
- Schwertmann, H.C.U., Cornell, R.M., 2000. *Iron Oxides in the Laboratory: Preparation and Characterization*. WILEY-VCH Verlag GmbH Germany.
- Sepúlveda, J., Gutiérrez, S., Vallette, M.C., Standen, V.G., Arriaza, B.T., Cárcamo-Vega, J.J., 2015. Micro-Raman spectral identification of manganese oxides black pigments in an archaeological context in Northern Chile. *Heritage Sci.* 3, 32.
- Sforza, M.C., Philippot, P., Somogyi, A., van Zuilen, M.A., Medjoubi, K., Schoep-Cohenet, B., Nitschke, W., Visscher, P.T., 2014. Evidence for arsenic metabolism and cycling by microorganisms 2.7 billion years ago. *Nat. Geosci.* 7 (11), 811–815.
- Straub, K.L., Benz, M., Schink, B., Widdel, F., 1996. Anaerobic, nitrate-dependent microbial oxidation of ferrous iron. *Appl. Environ. Microbiol.* 62, 1458–1460.
- Tebo, B.M., Johnson, H.A., McCarthy, J.K., Templeton, A.S., 2005. Geomicrobiology of manganese (II) oxidation. *Trends Microbiol.* 13 (9), 421–428.
- Vandieken, V., Pester, M., Finke, N., Hyun, J.-H., Friedrich, M.W., Loy, A., Thammrath, B., 2012. Three manganese oxide-rich marine sediments harbor similar communities of acetate-oxidizing manganese-reducing bacteria. *ISME J.* 6 (11), 2078–2090.
- Villalobos, M., Toner, B., Bargar, J., Sposito, G., 2003. Characterization of the manganese oxide produced by *Pseudomonas putida* strain MnB1. *Geochim. Cosmochim. Acta* 67 (14), 2649–2662.
- Wignall, P.B., Newton, R., 1998. Pyrite framboid diameter as a measure of oxygen deficiency in ancient mudrocks. *Am. J. Sci.* 298 (7), 537–552.
- Wittkop, C., Swanner, E.D., Grengs, A., Lambrecht, N., Fakhraee, M., Myrbo, A., Bray, A.W., Poulton, S.W., Katsev, S., 2020. Evaluating a primary carbonate pathway for manganese enrichments in reducing environments. *Earth Planet. Sci. Lett.* 538, 116201. <https://doi.org/10.1016/j.epsl.2020.116201>.
- Wu, C., Zhang, Z., Xiao, J., Fu, Y., Shao, S., Zheng, C., Yao, J., Xiao, C., 2016. Nanhuan manganese deposits within restricted basins of the southeastern Yangtze Platform, China: Constraints from geological and geochemical evidence. *Ore Geol. Rev.* 75, 76–99.
- Xiang, J., Chen, J., Bagas, L., Li, S., Wei, H., Chen, B., 2020. Southern China's manganese resource assessment: An overview of resource status, mineral system, and prediction model. *Ore Geol. Rev.* 116, 103261. <https://doi.org/10.1016/j.oregeorev.2019.103261>.
- Yu, H., Leadbetter, J.R., 2020. Bacterial chemolithoautotrophy via manganese oxidation. *Nature* 583 (7816), 453–458.
- Yu, W., Algeo, T.J., Du, Y., Maynard, B., Guo, H., Zhou, Q., Peng, T., Wang, P., Yuan, L., 2016. Genesis of Cryogenian Datangpo manganese deposit: Hydrothermal influence and episodic post-glacial ventilation of Nanhua Basin, South China. *Palaeogeogr. Palaeoclimatol. Palaeoecol.* 459, 321–337.
- Yu, W., Algeo, T.J., Du, Y., Zhou, Q., Wang, P., Xu, Y., Yuan, L., Pan, W., 2017. Newly discovered Sturtian cap carbonate in the Nanhua Basin, South China. *Precamb. Res.* 293, 112–130.
- Yu, W., Polgári, M., Gyollai, I., Fintor, K., Szabó, M., Kovács, I., Fekete, J., Du, Y., Zhou, Q., 2019. Microbial metallogenesis of Cryogenian manganese ore deposits in South China. *Precamb. Res.* 322, 122–135.
- Zeng, Y., Liu, W., Ceng, H., Zheng, R., Zhang, J., Li, X., Jiang, T., 1995. Evolution of Sedimentation and Tectonics of the Youjiang Composite Basin, South China. *Acta Geologica Sinica - English Ed.* 8, 358–371.